CONFINED AND UNCONFINED COMPRESSIVE STRENGTH AND DEFORMATION
OF CONCRETE AT HIGH STRAIN RATES

By

JHY-CHERNG GONG

A DISSERTATION PRESENTED TO THE GRADUATE SCHOOL OF
THE UNIVERSITY OF FLORIDA IN PARTIAL
FULFILLMENT OF THE REQUIREMENTS FOR THE DEGREE OF
DOCTOR OF PHILOSOPHY

UNIVERSITY OF FLORIDA

1988

TABLE OF CONTENTS

LIST OF TABLES

LIST OF FIGURES

vi

CONFINED AND UNCONFINED COMPRESSIVE STRENGTH AND DEFORMATION
OF CONCRETE AT HIGH STRAIN RATES

By

Jyh-Cherng Gong

August 1988

Dispersion of an elastic wave propagating in the transmitter bar
of the split Hopkinson pressure bars (SHPB) is studied with records
from two surface strain gage stations. The characteristics of
dispersion are demonstrated and discussed. Fourier series expansion
and the Fast Fourier Transform were employed along with numerical
results of the Pochhammer-Chree analysis of stress waves in an
infinitely long cylinder to reconstruct pulses from the SHPB. The
advantages of dispersion correction technique are demonstrated for
concrete specimens tested in the SHPB.

Extensive studies of uniaxial unconfined dynamic impact tests of
high strength concrete cylindrical specimens with a maximum aggregate
size 12.7 mm (0.5 inch) were performed with a 75 mm (3 inches)
diameter SHPB. Studies of the fracturing processes were carried out
with detailed and abundant information acquired from the SHPB results,

to which the dispersion correction technique was applied. Surface strain gages were mounted on some of the tested specimens. The recordings from these strain gages were studied in detail for the understanding of the failure processes. It was found that these gage records furnish valuable information in this study.

A new cementitious material system SIFCON (Slurry Infiltrated Concrete) was uniaxially impact tested with the SHPB. Its ductile response and damages were presented and investigated.

Passively confined dynamic impact experiments on plain concrete specimens were performed with steel and aluminum jackets and the SHPB. The specific requirements of the specimens employed in jacketed tests were achieved with metallic-mold casting. The confining pressures were obtained by mounting surface strain gages on the jackets. Permanent deformation and residual static strength were studied in the characterization of the behavior of plain concrete specimens under dynamic multiaxial loads.

CHAPTER I
INTRODUCTION

In the application of today's engineering materials, in addition
to the usual static properties, it is essential to know how these
materials behave under dynamic impact loads, since these materials are
very often subjected to non-static loading conditions during service.
Many types of instrumented impact testing apparatus have been
developed and employed to obtain either quantitative or qualitative
results. Most of these testing equipments measure only a very limited
number of parameters; e.g. notch bar impact tests (such as Izod or
Charpy impact tests) give specimen break energy alone and the falling
weight test measures solely specimen cracking energy. These
parameters may be useful in material screening and product quality
control, but they do not provide engineers with complete stress-
strain or stress-strain rate curves. It is highly desirable that from
a series of experiments one can eventually generate data for dynamic
constitutive models which could be applied in the increasingly popular
numerical simulations of engineering structures.

Since its introduction in 1949 by Kolsky [18], the split
Hopkinson pressure bars (SHPB) have been widely used in dynamic
compressive impact testing of metals, rock, and various materials. In
the past three decades, a variety of versions of the SHPB system have
been evolved and employed in dynamic tension and torsion tests also.

The standard compressive version of the SHPB consists of three

1

metallic long bars. The specimen of the material to be tested, of cylindrical shape, is sandwiched between two strain-gaged bars, called the incident and the transmitter bars. The third bar is the striker bar, which is driven pneumatically or mechanically with a controlled velocity and impacts the incident bar in the test. A compressive incident pulse is developed during the impact. This compressive incident pulse travels along the incident bar and, due to the differences of mechanical impedance of bar material and the specimen material, partly propagates through the specimen as a compressive pulse and partly reflects from the incident-specimen interface as a tensile pulse. Again, because of the differences of mechanical impedance a series of compressive waves, generated from the partly transmitted incident pulse and the specimen-transmitter bar interface, propagate back and forth in the specimen between the specimen-bar interfaces. The length of the specimen is supposed to be so small that these reflections lead to an approximately uniform stress along the specimen length and the impact to be so moderate that no shock wave effects occur.

Three pulses, namely incident, reflected, and transmitted pulses, are sensed by the strain gages mounted on the surface of the incident and transmitter bars and are recorded, through amplifiers, in the studies to be reported here with a digital electronic oscilloscope. From the analysis of these three pulses one is able to determine stress-time, strain-time, stress-strain, and strain rate-time curves. These results furnish abundant information for the study of dynamic impact properties of the tested material.

Most of the analyses of SHPB results have been based on several assumptions. One of these assumptions is that the one-dimensional wave theory is adequate in the interpretation of pulses traveling along the bars. In order to be more accurate in the analysis of test results, it is desirable to use a more general theory to take the dispersion into consideration for the larger-diameter bars which are employed in this research for the testing of concrete specimens.

This dissertation contains five chapters. Chapter 2 gives reviews of elastic longitudinal wave theories, which are fundamental in the application of the split Hopkinson pressure bars, and the configuration of the present SHPB system. Experiments and calculations involved in the dispersion investigation and reconstruction of waves are presented in Chapter 2 along with discussion on the studies performed.

A dynamic impact experimental study of high strength concrete using the SHPB and applying the dispersion correction techniques is described in Chapter 3. Detailed study of the failure processes of concrete specimens subjected to impact loads is also presented accompanied with proposed explanations in Chapter 3.

In Chapter 4, two sections on two distinct passive confined tests of cementitious materials are given. The experiments and results obtained on specimens of a new material system (SIFCON), which are made by infiltrating slurry into random short steel fiber preforms, are presented in the first section. For such a material system, the cementitious substance is passively confined by the short steel fiber preform when the specimen is deformed. Other passive confinement

tests, which were carried out employing metallic jackets, are described and discussed in the second section of Chapter 4. Some information on the dynamic behavior of plain concrete under multi-axial loading conditions is obtained with these jacketed confinement tests.

Conclusions are given at the ends of Chapters 2 and 3 and at the ends of the two sections of Chapter 4. A summary of the studies and conclusions is given in Chapter 5.

CHAPTER 2
DISPERSION INVESTIGATION OF WAVE PROPAGATION IN
THE SPLIT HOPKINSON PRESSURE BARS

2.1 Introduction

In 1914, Bertram Hopkinson [19] configured a cylindrical steel bar several feet in length and an inch in diameter to study the pressure-time relations of an explosive wave or of a projectile impingement that was applied to one end of the bar. This apparatus, which applied the simple theory of elastic wave propagation, has become known as the Hopkinson pressure bar.

Davies, in 1949 [9], substituted electrical condenser systems for the mechanical devices in the Hopkinson pressure bar and comprehensively studied the propagation of elastic stress waves in the Hopkinson pressure bar. From his experiments Davies concluded that in many instances dispersion plays an important role in the investigations of elastic stress pulses in a cylindrical bar. He further applied the numerical results calculated from the Pochhammer-Chree frequency equation to determine the dispersion of an elastic wave traveling a distance x along the Hopkinson pressure bar. In his study an assumed trapezoidal periodic wave was initiated at the end of the bar. He found that in the Hopkinson pressure bar test, the waves belong to the first mode of vibration. Davies' study showed the possibility to reconstruct a dispersive elastic stress wave along a cylindrical bar with the knowledge of the bar's radius, Young's modulus, Poisson's ratio, and density.

5

Yew and Chen [34] also experimentally demonstrated that the dispersive characteristics of longitudinal waves in a long aluminum cylinder belonged to the first mode vibration. They calculated the phase velocity-frequency relationship from two pulses recorded from two semiconductor-type strain gage stations on the surface of a 1.8 cm (0.75 in) diameter bar using the Fast Fourier Transform technique. The remarkable agreement of their phase velocity-frequency results with the first mode vibration results obtained from Pochhammer frequency equations has substantiated that the vibrations of an axially impacted long cylinder are first mode vibration.

In 1983, Follansbee and Frantz [12] repeated the calculation of the dispersive wave by Davies and used the technique to analyze results from a split Hopkinson pressure bar. A split Hopkinson pressure bar (SHPB) is a modified arrangement of two Hopkinson pressure bars, introduced by Kolsky in 1949 [18], which has been widely used for compressive tests of material properties at high strain rates, and is often called a Kolsky bar system. Follansbee and Frantz also demonstrated that the fundamental mode of vibration is excited in the impact tests of the split Hopkinson pressure bar. That the dispersion correction technique is able to reduce the magnitude of the oscillations of the stress strain curves for tested metals was proved as well.

Nevertheless, the complexity of the end conditions on the impact ends of the striker and incident bars may make it unsuitable to assume a trapezoidal wave initiated at the impact end of the incident bar as Follansbee and Frantz did in the SHPB.

In the following study, to demonstrate the dispersion correction, pulses are recorded at two stations on the transmitter bar of the SHPB. Station 1 is near the incident bar and station 2 is 1.27 meters further along. A data reduction computer code based on Fourier series expansion was acquired from Felice [10] and modified for the present SHPB system. Another numerical scheme using Fast Fourier Transform (FFT) was implemented as well, which runs more economically and accurately. The correction was applied in two ways. The pulse recorded at station 1 was time-shifted and dispersion-corrected to station 2, where it was compared with the actual pulse recorded at station 2. In the second application the wave recorded at station 2 was dispersion-corrected and time-shifted back to station 1 and compared with the actual recorded wave there. In recording these pulses the test is conducted with no specimen placed between incident and transmitter bars. The good agreement obtained again validates the assumption that the waves in the pressure bar follow the first mode dispersion. Examples of corrected and uncorrected pulses will be given in section 2.4.

The dispersion-correction procedure was then applied to the actual incident, reflected and transmitted pulses in tests with a concrete specimen in place. The dynamic stress-strain curves obtained in this way showed fewer oscillations than those which were not corrected for dispersion. Also, the stress-time curves at the two interfaces of the specimen agreed earlier in time than did the uncorrected curves.

2.2 Elastic Longitudinal Wave Theories
in A Long Cylinder

2.2.1 Simple One-Dimensional Theory

For a cylindrical rod, if its length is much larger than its diameter and the wave length of the stress pulse is much longer than the lateral dimension of the bar, the idealized one-dimensional wave theory is commonly adequate for elastic wave propagation study. The one dimensional wave equation is directly obtained by assuming that stress is uniformly applied over each cross-section and that plane cross sections remain plane during the motion. For a long cylindrical uniform bar with Young's modulus E and density ρ, the equation of motion derived from Newton's second law of motion, strain-displacement, and stress-strain relations can be written as

$$\rho \frac{\partial^2 u}{\partial t^2} = E \frac{\partial^2 u}{\partial z^2} \ . \tag{2-2-1}$$

In this equation, t is time, z is the coordinate along the longitudinal axis of bar and u is displacement in the z-direction. The solution of the above equation may be written as

$$u = f(c_0 t - z) + g(c_0 t + z), \tag{2-2-2}$$

where $c_0 = (E/\rho)^{1/2}$ is the bar wave speed, and f and g are two arbitrary functions depending on the initial conditions. The wave velocity here is dependent on the bar's elastic constant and density and assumed to be independent of the frequency of the stress waves.

From equation (2-2-2) the stress σ_z in a bar wave that propagates into an unstressed region in the positive z-direction can be derived as

$$\sigma_z = - \rho c_0 \frac{\partial u}{\partial t} \ . \tag{2-2-3}$$

According to this relation and equation (2-2-2), the longitudinal stress and displacement are uniform over the cross-section of the bar. Radial stress and the displacement in the radial direction are not considered in the one-dimensional wave theory.

Equations used in the calculation of stress-strain and stress-strain rate curves in the split Hopkinson pressure bar tests have usually been based on this simple wave theory of a cylindrical bar. The wave initiated by the impact of the striker bar on one end of the incident bar is assumed to travel through the incident bar without any phase change or distortion. So the incident pulse at the specimen interface is considered to be the same as the wave which is recorded at a distance ahead of the incident bar-specimen interface. Also the pulse which passes through the specimen is thought to be the same as the wave recorded down at the middle of the transmitter bar. The same story applies for the reflected wave. The simple wave theory may still be a good approximation if the force producing the pulse is applied relatively slowly and uniformly in a long slender bar. When the loading speed and force are increased the real wave propagation may deviate from the one dimensional idealization. In such circumstances, application of a more general longitudinal elastic wave theory to obtain a dispersion correction for the one-dimensional

analysis of the split Hopkinson pressure bar seems mandatory for more
accurate results. It is especially important when the incident and
reflected pulses are of comparable magnitude. In this situation
dispersion effects are especially noticeable when the two waves are
added algebraically to get the stress at the specimen interface with
the incident pressure bar.

2.2.2 More General Theory (Pochhammer-Chree Analysis)

In solving wave problems of a cylinder [19], the equations of
motion in Cartesian coordinates are transformed into cylindrical polar
coordinates for easy manipulation with boundary conditions. By taking
the z-axis along the cylinder axis and assuming that particles vibrate
only in r-z plane and the motion is symmetric about the z-axis, i.e.
the displacement in the circumferential direction vanishes, the
equations of motion in cylindrical coordinates can be derived as

$$\rho \; \frac{\partial^2 u_r}{\partial t^2} \; = \; (\lambda+2\mu) \; \frac{\partial \Delta}{\partial r} \; + \; 2\mu \; \frac{\partial \Omega}{\partial z} \; , \qquad (2\text{-}2\text{-}4)$$

$$\rho \; \frac{\partial^2 u_z}{\partial t^2} \; = \; (\lambda+2\mu) \; \frac{\partial \Delta}{\partial z} \; - \; (2\mu/r) \; \frac{\partial (r\Omega)}{\partial r} \; . \qquad (2\text{-}2\text{-}5)$$

In these equations t is time, u_r and u_z are radial and axial
displacement, respectively, ρ is the density, λ and μ are Lame'
constants, and Δ and Ω are defined as

$$\Delta = \frac{1}{r} \frac{\partial(ru_r)}{\partial r} + \frac{\partial u_z}{\partial z} , \qquad (2\text{-}2\text{-}6)$$

$$\Omega = \frac{1}{2} (\frac{\partial u_r}{\partial z} - \frac{\partial u_z}{\partial r}). \qquad (2\text{-}2\text{-}7)$$

For a wave propagating in the positive z direction, assume that u_r and u_z are simple harmonic functions of z and t and of the form

$$u_r = U \exp [(ct - z) 2\pi i/\Lambda], \qquad (2\text{-}2\text{-}8)$$

$$u_z = W \exp [(ct - z) 2\pi i/\Lambda], \qquad (2\text{-}2\text{-}9)$$

in which U and W are two functions of the radial coordinate r, while c and Λ are the phase velocity and wavelength of a propagating longitudinal harmonic elastic wave in a cylinder and $i = (-1)^{1/2}$. Substituting these two assumed displacements into equations (2-2-4) and (2-2-5) leads to

$$\frac{\partial^2 \Delta}{\partial r^2} + \frac{1}{r} \frac{\partial \Delta}{\partial r} + h^2 \Delta = 0 , \qquad (2\text{-}2\text{-}10)$$

and

$$\frac{\partial^2 \Omega}{\partial r^2} + \frac{1}{r} \frac{\partial \Omega}{\partial r} - \frac{\Omega}{r^2} + k^2 \Omega = 0 , \qquad (2\text{-}2\text{-}11)$$

where

$$h^2 = (2\pi/\Lambda)^2 (\frac{\rho c^2}{\lambda+2\mu} - 1) , \qquad (2\text{-}2\text{-}12)$$

$$k^2 = (2\pi/\Lambda)^2 (\frac{\rho c^2}{\mu} - 1) . \qquad (2\text{-}2\text{-}13)$$

The stress components σ_{zz}, σ_{rr}, and σ_{rz} related to the displacements by the stress-strain equations can be written as

$$\sigma_{zz} = \frac{\lambda}{r} \frac{\partial(ru_r)}{\partial r} + (\lambda+2\mu) \frac{\partial u_z}{\partial z} , \qquad (2-2-14)$$

$$\sigma_{rr} = (\lambda+2\mu) \frac{\partial u_r}{\partial r} + \lambda \left(\frac{u_r}{r} + \frac{\partial u_z}{\partial z} \right) , \qquad (2-2-15)$$

$$\sigma_{rz} = \mu \left(\frac{\partial u_r}{\partial z} + \frac{\partial u_z}{\partial r} \right) . \qquad (2-2-16)$$

In this more general longitudinal elastic wave analysis, the longitudinal stress and displacement vary over the cross-section of the cylinder, the radial stress is no more zero as in one-dimensional analysis, except at the free lateral surface, and the displacement varies non-linearly in the radial direction.

By solving equations (2-2-10), (2-2-11) and applying boundary condition that σ_{rr} and σ_{rz} vanish at the lateral surface of the cylinder, the following equations can be obtained.

$$2A \left(\frac{2\pi}{\Lambda}\right) \frac{\partial J_0(ha)}{\partial a} + B\left(\frac{2\pi}{\Lambda}\right)^2 (2 - \frac{\rho c^2}{\mu}) J_1(ka) = 0 , \qquad (2-2-17)$$

$$A \left[2\mu \frac{\partial^2 J_0(ha)}{\partial a^2} - \frac{\lambda\rho}{\lambda+2\mu} \left(\frac{2\pi c}{\Lambda}\right)^2 J_0(ha) \right]$$

$$+ 2B\mu \left(\frac{2\pi}{\Lambda}\right) \frac{\partial J_1(ka)}{\partial a} = 0 , \qquad (2-2-18)$$

where a is the radius of the cylinder and J_0 and J_1 are Bessel's functions of order zero and one, respectively. On eliminating constants A and B from the above equations, an equation involving the wavelength of the vibrations, the elastic constants, and the radius and density of the cylinder can be obtained. This equation takes the form

$$
\begin{vmatrix}
2 \ (\frac{2\pi}{\Lambda}) \ \frac{\partial \ J_0(ha)}{\partial a} & (\frac{2\pi}{\Lambda})^2 (2 \ - \ \frac{\rho c^2}{\mu}) \ J_1(ka) \\[3mm]
2\mu \ \frac{\partial^2 J_0(ha)}{\partial a^2} \ - \ \frac{\Lambda \rho}{\Lambda + 2\mu} \ (\frac{2\pi c}{\Lambda})^2 J_0(ha) & 2\mu \ (\frac{2\pi}{\Lambda}) \ \frac{\partial J_1(ka)}{\partial a}
\end{vmatrix} = 0 \ ,
$$

(2-2-19)

which is known as the frequency equation. This equation can be solved for the phase velocities c_n of sinusoidal waves with any frequency f_n and wave length Λ_n along an infinitely long cylinder. It comes out a function with non-dimensional variables of phase velocity, wavelength, and the Poisson's ratio ν, elastic modulus E, and radius of the cylinder a, which can be expressed as

$$
c_n \ / \ c_0 = D \ (a/\Lambda_n \ , \ \nu), \tag{2-2-20}
$$

where $c_0 = (E/\rho)^{1/2}$, $c_n = f_n \ \Lambda_n$, and D is a certain nonlinear function.

The above solution scheme was presented by Pochhammer in 1876 as well as by Chree in 1889 independently. Solutions so obtained are for

an infinitely long cylinder and are not exact for finite cylinders, since the boundary conditions at the ends of the cylinder cannot be fulfilled by these solutions. However, they can more precisely characterize the elastic wave propagation behavior along the cylinder than the one-dimensional approximations.

Given the Poisson's ratio, equation (2-2-20) can be solved for multiple roots which differ from zero. Each set of these roots corresponds to a different mode of vibration of the cylinder. The particular mode of vibration will depend on the initial conditions. It was verified by Davies experimentally that the first mode vibration is usually excited in the Hopkinson pressure bar tests. Numerical results of the first three modes in a cylinder with Poisson ratio 0.29 were calculated by Davies [9] in 1949. Bancroft [2], on the other hand, calculated the first mode vibration for a series of Poisson's ratios, and the curve interpolated from his results for Poisson's ratio of 0.29 agrees with Davies' results. By applying these numerical results, the phase velocity of any wave length can be calculated and the phase angle changes in the propagation of an elastic wave can be predicted at any position. Dispersion correction is thus made possible.

2.3   The Split Hopkinson Pressure Bars

2.3.1 Equipment

Figure 2-1 is a schematic of the SHPB used in the current study. The whole system is located at the Department of Aerospace Engineering, Mechanics, and Engineering Science, University of
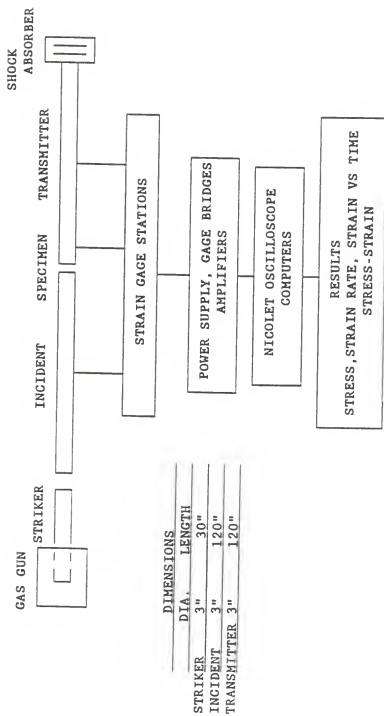
Figure 2-1. Schematic of the split Hopkinson pressure bars used in this study.

Florida. The striker bar is propelled by a compressed-nitrogen-charged gas gun to impact axially the incident bar which transmits the loading pulse to the specimen sandwiched between the incident bar and the transmitter bar. A shock absorber is built behind the transmitter bar to absorb post-test system momentum.

Three gage stations are permanently mounted on the system. One of them is on the incident bar 1.524 meters from the specimen interface, the other two stations are on the transmitter bar. The first gage station on the transmitter bar is 0.254 meter from the specimen interface and the second one is 1.27 meters down along the bar. Each station has four double strain gage rosettes (Micro-Measurements Type WA-06-250TB-350) mounted 90 degrees apart circumferentially. The gages of each rosette are oriented along with the longitudinal and transverse directions of the bar. Two of the four rosettes which are opposite to each other on each station are bridged to the power supply and the amplifier. The other two rosettes of each gage station are spare. A four-channel Nicolet 4094 digital storage oscilloscope is used to record and store pulses. Subsequent manipulations of the recorded data are performed in digital computers.

3-2. Analysis

From equation (2-2-3) a relationship between the particle velocity and the strain of a longitudinal elastic pulse, based on the idealized one-dimensional wave analysis, propagating in the positive direction in a cylinder can be derived as

$$V = -c_0 \epsilon$$

(2-3-1)

In a SHPB system the specimen is closely placed between the incident and the transmitter bars. The rate of deformation of a specimen tested in the SHPB can be expressed as

$$V_s = V_1 - V_2 = - c_0 (\epsilon_I - \epsilon_R - \epsilon_T), \qquad (2-3-2)$$

where
$$V_1 = - c_0 (\epsilon_I - \epsilon_R), \qquad (2-3-3)$$

and
$$V_2 = - c_0 \epsilon_T, \qquad (2-3-4)$$

are the particle velocities at the incident interface and the transmitter interface respectively. In the above equations ϵ_I, ϵ_R, and ϵ_T are strains of the incident pulse, the reflected pulse, and the transmitter pulse. For a specimen with initial length L_0, the nominal strain rate $\dot{\epsilon}_s$ is $(V_1 - V_2)/L_0$ or

$$\dot{\epsilon}_s = - c_0 (\epsilon_I - \epsilon_R - \epsilon_T)/ L_0. \qquad (2-3-5)$$

The strain of a specimen can be obtained by integrating equation (2-3-5) with time.

By Newton's Third Law at the specimen-bar interfaces, the stresses of the specimen at the incident bar interface and at the transmitter bar interface, σ_1 and σ_2 , can be obtained. They are

$$\sigma_1 = E (A/A_s) (\epsilon_I + \epsilon_R), \qquad (2-3-6)$$

$$\sigma_2 = E \ (A/A_s) \ \epsilon_T \ , \qquad (2-3-7)$$

where A and A_s are the cross-section area of the SHPB and the specimen. An estimate of the average stress along the specimen length can be given by

$$(\sigma_s)_{AV} = \ (\sigma_1 + \sigma_2 \ )/2 \ . \qquad (2-3-8)$$

From the above analysis the stress-time, strain-time, strain rate-time, and stress-strain curves of a tested specimen can be obtained.

2.4 Experiments, Calculations and Results

2.4.1 Determination of Pulse Width, Wave Speed, and Poisson's Ratio of the SHPB System

From equation (2-2-20), material properties E, ρ, and ν of the SHPB have to be determined to perform dispersion corrections. Tests were conducted with the three-inch diameter bar system at the University of Florida to measure wave speed and Poisson's ratio. At the beginning of these measurements, with no specimen in place, a pulse in the incident bar was generated with an arbitrary striker-bar impact speed and reflected from the free end of the bar. The reflected tension pulse propagates back to the impact end, which is free from the striker bar right after the first pulse was produced, and reflects as a compression pulse. A series of compression-tension pulses will travel forward and backward in the incident bar. If the sampling period in the Nicolet is set to 1.0 microsecond, a total of six pulses can be recorded. Figure 2-2 shows five of the six recorded
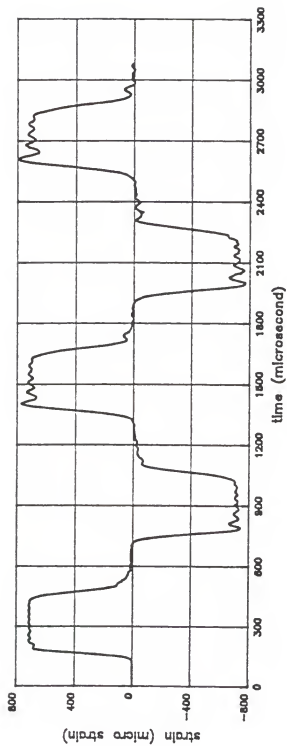
Figure 2-2. Incident pulse as it initially arrives and after four reflections from free ends.

pulses. The pulse amplitudes were determined by averaging the pulse height for a 200 microsecond span following the first peak of each pulse. As so determined, the pulse amplitudes were all 710.5±3.5 microstrain. The pulse widths measured at points of 0.707 average amplitude of each pulse are 286.5±4.5 microseconds. Table 2-1 gives individual pulse amplitudes and widths. This shows that the main pulse amplitude and width are not affected by the dispersion, but, as can be seen in the figure, the oscillations superimposed on the main pulse change as the pulse propagates.

Table 2-1. Amplitude and width of initial incident pulse and five reflections.

Pulse No.	Character (C or T)	Amplitude ($\mu\epsilon$)	Width at .707 Amp. (μs)
1	C	706.10	291.0
2	T	709.58	289.0
3	C	709.46	286.0
4	T	710.96	285.0
5	C	709.05	282.0
6	T	709.02	282.0

The wave speed was determined from pulses recorded at the two stations on the transmitter bar. In recording these two pulses the incident bar and the transmitter bar were accurately aligned and in close contact with each other. Time for a wave to travel the distance between the two stations was determined by using the Nicolet program (#13) to shift the second pulse back to the first station and have two pulses match with each other as close as possible in their widths. The wave speed so determined is 5183.7 m/s for the present system.

Poisson's ratio was determined by the ratio of lateral and longitudinal strains, which were recorded at the gage station on the incident bar. The two gages used to record these two strains are on the opposite faces of the incident bar. The Poisson's ratio so determined was 0.32, which agrees with the vendor supplied value.

4-2. Phase Velocity versus Wave Length Interpolation Formula

The phase velocities of wave lengths for the current Poisson's ratio were interpolated from Bancroft's results. Table 2-2 shows the data calculated by Bancroft of Poisson's ratios 0.30 and 0.35 and the interpolated values for 0.32 Poisson's ratio. An algebraic formula that fits Davies' results, where radius/wave length (a/Λ_n) was used as abscissa, for Poisson's ratio 0.29 was acquired from Felice [10], which is

$$c_n / c_0 = 0.5764 + 0.4236 / [\ A_1(\tfrac{a}{\Lambda})^4 + A_2(\tfrac{a}{\Lambda})^3 + A_3(\tfrac{a}{\Lambda})^2 + A_4(\tfrac{a}{\Lambda})^{1.5} + 1\ ],$$

$$(2-4-1)$$

where $A_1 = 22.0$, $A_2 = 12.8$, $A_3 = -2.77$, and $A_4 = 0.92$.

A different set of constants that makes the formula fit the data points for Poisson's ratio 0.32 was calculated by a nonlinear least square curve fitting library code at NERDC in the University of Florida campus. The independent variable in this formula is changed to diameter/wave length (d/Λ_n), which was used in the Bancroft's calculations. The constants obtained are $A_1 = 2.148$, $A_2 = 0.736$, $A_3 = -0.276$, and $A_4 = 0.3065$. Figure 2-3 shows the interpolated points and the fitting curve for c_n/c_0 versus d/Λ_n.

Table 2-2. c_0/c_n as a function of d/Λ_n and ν.

d/Λ_n	Poisson's Ratios		
	0.30	0.32	0.35
0.000	1.000000	1.000000	1.000000
0.050	0.999440	0.999360	0.999240
0.100	0.997740	0.997420	0.996940
0.150	0.994820	0.994100	0.993020
0.200	0.990540	0.989252	0.987320
0.250	0.984660	0.982664	0.979670
0.300	0.976910	0.974062	0.969790
0.350	0.966880	0.963084	0.957390
0.400	0.954100	0.949332	0.942180
0.450	0.938100	0.932448	0.923970
0.500	0.918540	0.912232	0.902770
0.550	0.895490	0.888890	0.878990
0.600	0.869640	0.863148	0.853410
0.650	0.842220	0.836168	0.827090
0.700	0.814660	0.809236	0.801100
0.750	0.788180	0.783436	0.776320
0.800	0.763570	0.759462	0.753300
0.850	0.741250	0.737694	0.732360
0.900	0.721300	0.718200	0.713550
0.950	0.703650	0.700918	0.696820
1.000	0.688040	0.685876	0.682030
1.200	0.643240	0.641420	0.638690
1.400	0.646870	0.633258	0.612840
1.600	0.601110	0.599518	0.597130
1.800	0.591390	0.589758	0.587310
2.000	0.585240	0.583548	0.581010
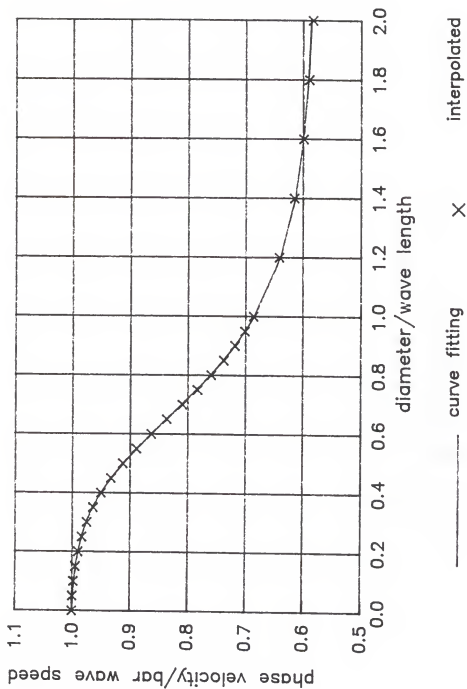
Figure 2-3. Phase velocity of first mode vibration versus wave length in cylindrical bar with 0.32 Poisson's ratio.

2.4.3 Numerical Scheme of Wave Transform and Reconstruction

2.4.3.1 Fourier Series Expansion

In the original investigations of Pochhammer and Chree the frequency equation applied to infinitely long continuous sinusoidal waves of various wave lengths. For application to a single pulse in a pressure bar it is necessary to represent the pulse in terms of its Fourier components. For a single pulse this could in principle be done by a Fourier integral transform technique in which the frequency is a continuous variable. Davies [9] and Follansbee and Frantz [12] chose instead to use a Fourier series expansion. Follansbee and Frantz chose a base period T long enough to contain the whole pulse. The Fourier series expansion then actually represents not just the single pulse but a periodic function which repeats the single pulse in every time interval of length T from negative infinity to positive infinity. The lowest angular frequency ω_0 in the representation is ω_0 = $2\pi/T$. In the series there is a discrete set of angular frequencies $\omega_n = n\omega_0$ for integers n from 0 to ∞. In practice the series is truncated at some finite value of n.

The Fourier series for the periodic function f(t) is assumed in the form

$$f(t) = A_0/2 + \sum_{n=1}^{\infty} D_n \cos(n\omega_0 t - \phi_n), \qquad (2\text{-}4\text{-}2)$$

where A_0, D_n are Fourier coefficients, ω_0 is the natural frequency, and ϕ_n is the phase angle. The coefficients D_n and ϕ_n are related to the usual Fourier coefficients A_n and B_n on an interval of length T by $D_n = (A_n^2 + B_n^2)^{1/2}$ and $\cos\phi_n = A_n/D_n$.

2.4.3.2 Fast Fourier Transform

A continuous wave, either periodic or non-periodic, can be aliased and Nyquist sampled to form a finite discrete Fourier transform (DFT) pair [5,6,7]. The discrete Fourier transform can be applied directly to digitally recorded pulses. The DFT is defined by

$$G_r = \sum_{k=0}^{N-1} F_k W_N^{rk}, \quad r=0,\ldots, N-1, \tag{2-4-3}$$

where $W_N = \exp(-2\pi i/N)$.

In this definition G_r is the rth coefficient of the DFT and F_k denotes the kth sample of the series which consists of N samples and $i = (-1)^{1/2}$. The integers k and r are the counterparts of times and frequencies respectively in a Fourier transform pair. The inverse of (2-4-3) is

$$F_k = (1/N) \sum_{r=0}^{N-1} G_r W_N^{-rk}, \quad k=0,\ldots,N-1. \tag{2-4-4}$$

The above relationship is called the inverse discrete Fourier transform (IDFT).

Most approaches to improving the efficiency of the computation of the DFT have exploited the symmetric and periodic properties of the complex sequence W. The fundamental principle that fast Fourier transform (FFT) algorithms are based upon is that of decomposing the computation of the DFT of a sequence of certain length into successively smaller DFTs. The FFT not only reduces the computation time; it also substantially reduces round-off errors associated with computations.

By considering the special case of N, in equation (2-4-3), an integer m power of 2, the computation of G_r can be performed by separating F_k into two N/2-point sequences consisting of the even-numbered points in F_k and the odd-numbered points in F_k. So

$$G_r = \sum_{k \text{ even}} F_k W^{rk} + \sum_{k \text{ odd}} F_k W^{rk} \qquad (2\text{-}4\text{-}5)$$

$$= \sum_{k=0}^{(N/2-1)} F_{2k}(W_N^2)^{kr} + W_N^r \sum_{k=0}^{(N/2-1)} F_{2k+1}(W_N^2)^{kr}.$$

Since $\qquad W_N^2 = \exp[-2i(2\pi/N)] = \exp[-2\pi i/(N/2)] = W_{N/2},\qquad (2\text{-}4\text{-}6)$

equation (2-4-5) can be written as

$$G_r = \sum_{k=0}^{(N/2-1)} F_{2k}(W_{N/2})^{kr} + W_N^r \sum_{k=0}^{(N/2-1)} F_{2k+1}(W_{N/2})^{kr}$$

$$\qquad (2\text{-}4\text{-}7)$$

$$= \qquad H_k \qquad + \qquad W_N^r I_k.$$

When N is equal to a power of 2, then N/2, N/4,..., and $N/(2)^{m-1}$ are integer powers of 2 as well. By the same considerations H_k and I_k in equation (2-4-7) can be further decomposed into computation pairs. And the DFT computations can eventually consist of m steps of pairs of two-point DFTs. A two point DFT is expressed as

$$G_r = H_k + W_N^r I_k, \quad r=0,1; \ k=0,1; \text{ and } N=2. \qquad (2\text{-}4\text{-}8)$$

Here $W_N^r = 1$ or -1.

By implementing the above algorithm, the transform sequence G_r consisting of pairs of real and imaginary parts can be readily calculated.

2.4.3.3 Calculation of Phase Angles and Reconstruction of Waves

The phase velocity of frequency component f_n is

$$c_n = f_n \Lambda_n = (n\omega_0/2\pi)\Lambda_n, \qquad (2\text{-}4\text{-}9)$$

where Λ_n is the wavelength corresponding to frequency f_n and $n\omega_0$ is angular frequency. Equation (2-4-9) can be non-dimensionalized, and gives

$$2\pi(c_n/c_0)(d/\Lambda_n) = n\omega_0(d/c_0). \qquad (2\text{-}4\text{-}10)$$

From this equation associated with the algebraic equation (2-4-1), phase velocities c_n can be determined for the Fourier components of a longitudinal wave traveling in the bar.

If there were no dispersion and all wave components traveled at the same speed c_0 , then the whole pulse would travel distance x in time x/c_0. With dispersion, a particular frequency component will travel at the speed c_n instead of c_0 , and this component will travel distance x in time x/c_n. The phase angle difference of this particular component from those components that travel with no dispersion will be

$$\phi_{dn} = n\omega_0(x/c_n - x/c_0) = (n\omega_0 x/c_0)[(c_0/c_n) -1]. \qquad (2\text{-}4\text{-}11)$$

By this equation and equations (2-4-1) and (2-4-10) the phase shift angle of each frequency component f_n of a dispersive pulse in a

cylinder can be obtained. The new phase angle for dispersive components that have traveled distance x are

$$\phi'_n = \phi_n + \phi_{dn} . \qquad (2-4-12)$$

With the corrected phase angles, pulses can be reconstructed either backward or forward in a long cylinder.

For the present dispersion study, with the pulse recorded from station 1 of the transmitter bar, x is 1.27 meters in the correction process, if it is to be corrected to the station 2 of the transmitter bar. If the corrections are performed opposite to the wave propagation direction, negative values of x have to be employed. For SHPB tests, in the reconstruction of the incident pulses positive x is used and it was 1.524 meters for the current system. For the reflected and transmitted pulses, the reconstructions are carried out opposite to the wave travel directions, so -1.524 meters was used.

In the Fourier series expansion scheme the whole pulse can be expressed as

$$f(t) = A_0/2 + \sum_{n=1}^{\infty} D_n \cos (n\omega_0 t - \phi'_n) \qquad (2-4-13)$$

after it travels distance x.

In the fast Fourier transform scheme the phase angles ϕ_n of the sampled points were found by $\cos \phi_n = RE/(IM^2+RE^2)^{1/2}$, where RE and IM are real and imaginary parts of G_r in equation (2-4-3). The calculated phase angles were then corrected for phase angle differences ϕ_{dn}. With the new phase angles and the preserved amplitudes, which are equal to $(IM^2+RE^2)^{1/2}$, a reconstructed pulse at distance x was obtained by the inverse FFT.

2.4.4 Experiments and Results

In order to investigate wave dispersion characteristics two pulses were recorded from two stations 1.27 meters apart on the transmitter bar. Figure 2-4 shows the two recorded pulses plotted versus time. For easy and precise study the pulses recorded from the second station were shifted in time to the first pulses, as shown in Figure 2-5. Figure 2-6 presents the comparison of the original recorded pulse at station 2 (solid line) and the forward-dispersion-corrected pulse (dashed line) of the pulse recorded at station 1 obtained through the application of the FFT scheme. Figure 2-7 shows the plots of original recorded pulse at station 1 (solid line) and the backward-dispersion-corrected pulse (dashed line) of the pulse recorded at station 2 obtained by employing the Fourier series expansion technique. Figure 2-8 compares the forward-dispersion corrected pulses from the recorded pulse at station 1 obtained by using the FFT and the Fourier series expansion respectively.

The Fourier series expansion technique was applied to the incident, the reflected, and the transmitted pulses of a concrete experiment. Figure 2-9 gives the recorded raw pulses of a tested concrete specimen which had two mounted surface strain gages. Figure 2-10 shows the plots of the time-shifted corrected and uncorrected incident, reflected, and transmitted pulses. Figure 2-11 (right) shows the comparison of two stresses at the specimen interfaces, which were calculated from the original recorded incident, reflected, and transmitted pulses, while Figure 2-11 (left) shows interface stresses, which were obtained through the dispersion corrected incident,
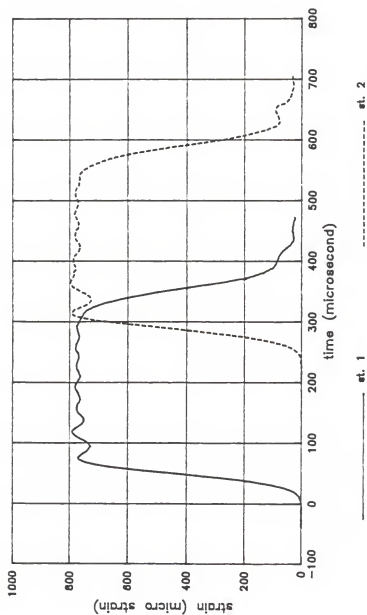
Figure 2-4. Uncorrected pulses at two stations on the transmitter bar as actually recorded.

Figure 2-6. Dispersion-corrected station 1 pulse of Fig. 2-4 using the FFT and uncorrected station 2 pulse.

Figure 2-5. Uncorrected pulses of Fig. 2-4 with station 2 pulse time-shifted back to station 1.

Figure 2-8. Dispersion-corrected station
1 pulses from the FFT and Fourier series
expansion respectively station 1 pulse.

Figure 2-7. Dispersion-corrected station
2 pulse of Fig. 2-4 from Fourier series
expansion technique and recorded station
1 pulse.
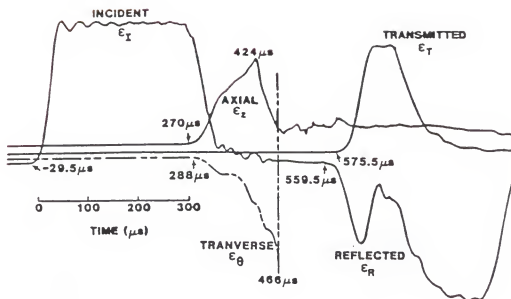
Figure 2-9.   Strain Pulses in Pressure Bars and Axial and
                Lateral Specimen Surface Strains.
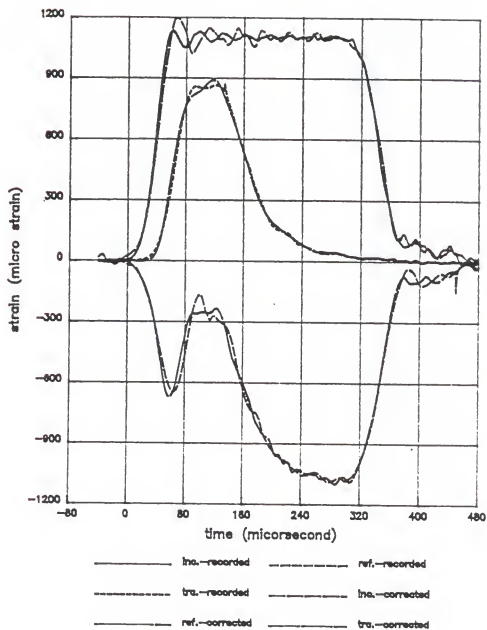
Figure 2-10. Incident, reflected and transmitted pulses (corrected and uncorrected) for the SHPB test.
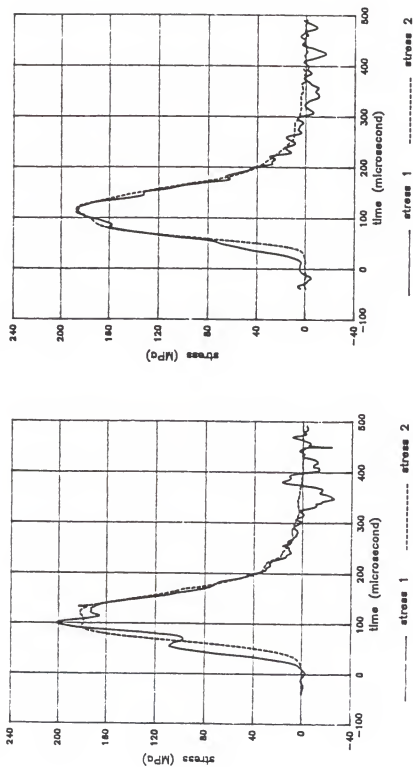
Figure 2-11. Uncorrected stress-time curves (right) and the corrected curves (left) at two interfaces.

reflected, and transmitted pulses. More results of interface stresses on concrete specimens will be shown in the next chapter. Figure 2-12 compares corrected and uncorrected stress-strain curves.

2.5 Discussion

From Table 2-1 and Figure 2-2 the main pulse amplitudes of a train of pulses are apparently not affected by the dispersion. The pulse widths seemed getting smaller for pulses with more reflections, though the differences are not significant. By careful examination of the oscillations on the top of each pulse, it is not difficult to find out that the number of these oscillations decreased as the wave propagated. The dispersive character, as well as wave reflection from free ends of a long cylinder, account for this reduced number of oscillations. It is also found that the oscillations trailing each pulse increased as the wave propagates. This phenomenon manifests that the oscillations which belong to high frequency components traveled slower and have lagged behind in a dispersive medium. The same conclusion can also be drawn from close observation of the two pulses consecutively recorded on the transmitter bar in Figures 2-4 and 2-5. From Figure 2-5 the out-of-phase superimposed oscillations and the lagging of each individual oscillation of the second pulse (dashed line) to the first pulse (solid line) give a further verification of the conclusion.

Follansbee and Frantz [12] demonstrated that the vibrations of an impact test belong to the first mode vibration through the evidences of 1. agreement between the measured incident pulse and the predicted
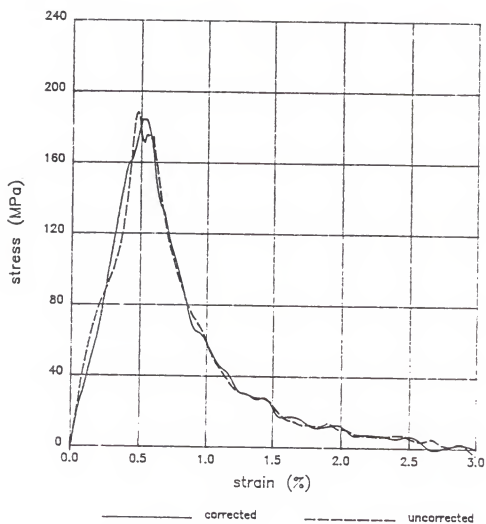
Figure 2-12. Corrected and uncorrected stress-strain curves.

incident pulse, which was obtained by assuming a trapezoidal wave initiated at the impact end and 2. the excellent correspondence in time of the peaks and valleys of incident and reflected pulses which were both dispersion corrected to the incident bar/specimen interface. In a real impact test, the complex impact end conditions do not provide a solid fundation for making the trapezoidal initial pulse assumption. In addition, the configuration of such an assumed pulse may further complicate the problem.

The study of two consecutively recorded pulses on the transmitter bar has been exempted from the problems of assuming an initial trapezoidal wave. The agreement of a real recorded pulse at a position and a second pulse which is dispersion corrected to the first position from a recorded pulse at a second position (Figures 2-6, 2-7) by assuming the dominance of the first mode vibration in a SHPB test gave a good evidence that mode one vibration is the origin of oscillations. It also was verified in the study by Yew and Chen [34] and in the present study that the dispersion correction based on the frequency equation for an infinite bar can be applied to a propagating pulse at two stations on a finite bar so long as reflections from the bar ends do not interfere with the pulse.

From Figure 2-8, it seems that the employed numerical scheme in the dispersion correction technique does not make any difference on the calculated results. Nevertheless, since far fewer algebraic manipulations are involved in the FFT, the round-off errors as well as the computer time required have been significantly reduced as compared to the Fourier series expansion scheme. (In the present study the

computer time ratio for two schemes is approximately 1:10 in an IBM PC-XT compatible with 8 MHz clock frequency and an Intel 8087 mathematical coprocessor.)

The forward-dispersion corrected incident pulse and backward-dispersion corrected reflected pulse of a concrete experiment in Figure 2-9 show again the characteristics of the previous conclusions that the high frequency components of a wave lag behind as the wave propagates and the oscillations of an impact test belong to the first mode vibration.

Table 2-3 gives the radius/wave length ratios and the corresponding Fourier series coefficient ratios for the first 20 frequency components of three incident pulses which were used in the tests of specimens 03w, 01w, and 02w for the present SHPB system. The striker-bar impact velocities of these three incident pulses are 5.87 m/s, 12.85 m/s, and 17.12 m/s. The ratio of radius and wave length gets larger than 0.10 after n=6; at that moment the ratio of Fourier components to the largest component falls between 0.032-0.056. For higher impact velocities, the incident pulses consist of more high frequency components. This can also be observed from the oscillations on the top of incident pulses.

Davies [9] calculated from Pochhammer-Chree Analysis and concluded that for $a/\Lambda_n < 0.10$, where a is bar's radius, the difference of longitudinal displacement at the bar surface and that at the bar axis can be as much as five percent for one frequency component. When a/Λ_n becomes large, Davies also concluded that for some components the longitudinal displacement changes its sign from

the bar surface to its center. The amount of nonuniformity in the profiles of the longitudinal stress and displacement depends on the combined effects of the displacement of each frequency component and the magnitude of the corresponding Fourier coefficients. Because the Fourier coefficients of higher frequency components are comparatively smaller, the longitudinal displacement profile of the sum should not be seriously affected by the nonuniform longitudinal displacement of these higher frequency components. Detailed quantitative study, which calculates the total displacement profile by summing the individual components as functions of r would give a more precise conclusion.

2.6 Conclusions

The dispersive characteristics of a longitudinal elastic wave propagating in a long cylindrical bar were shown experimentally with two consecutive pulses travelling in the transmitter bar of the SHPB. This experiment eliminated the problems of assuming an initial trapezoidal excitation. High frequency components were found to lag behind lower frequency components, and this lag is attributed to the characteristics of dispersion. These high frequency oscillations, however, did not have any influence on the main pulse width.

Numerical results of the first mode vibration of Pochhammer-Chree analysis of elastic waves in a cylinder were employed along with a recorded pulse to reconstruct the pulse at a second position along the bar. It was shown that the dispersion correction technique can accurately reconstruct pulses along the cylinder from a pulse which is recorded in another location on the cylinder. This pulse

Table 2-3. Radius to wave length ratios and the associated
Fourier series coefficient ratios for the
incident pulse of a 76.2 mm diameter SHPB.

	D_n/A_0 of ϵ_I		
n	a/Λ_n	03w	01w	02w
1	0.01440	0.44721	0.47869	0.49080
2	0.02880	0.13468	0.13791	0.14046
3	0.04325	0.06961	0.08946	0.09296
4	0.05770	0.07365	0.09381	0.09984
5	0.07230	0.00967	0.01274	0.01456
6	0.08690	0.03187	0.04891	0.05578
7	0.10170	0.01535	0.02064	0.02386
8	0.11660	0.01178	0.02265	0.02256
9	0.13175	0.01366	0.02416	0.02610
10	0.14720	0.00474	0.00872	0.01282
11	0.16299	0.00466	0.00932	0.01441
12	0.17929	0.00343	0.00908	0.01033
13	0.19619	0.00246	0.00842	0.01011
14	0.21394	0.00289	0.00583	0.00962
15	0.23279	0.00173	0.00321	0.00392
16	0.25303	0.00081	0.00534	0.00478
17	0.27514	0.00182	0.00114	0.00300
18	0.29969	0.00040	0.00391	0.00359
19	0.32730	0.00082	0.00152	0.00258
20	0.35855	0.00079	0.00106	0.00326

pulse from time domain to frequency domain, the reconstruction of new phase angles of a second position, and the inverse transforming of the new pulse from frequency domain to time domain. The transforming of pulses were successfully done with the FFT, which needed much less computer time than the Fourier series expansion scheme and is believed also to give more accurate results.

The dispersion correction technique was employed to analyze concrete specimen test results. From the close agreement of specimen-bar interface stresses, the merits of this technique were demonstrated.

CHAPTER 3
UNCONFINED DYNAMIC UNIAXIAL COMPRESSIVE STRENGTH AND
DEFORMATION OF CONCRETE

3.1 Introduction

Only with a comprehensive knowledge of the mechanical behavior of
concrete can engineers optimize the usage of this engineering
material. While numerous static test data of concrete have been
published, comparatively little results have been given on its dynamic
performance. At present there is still no universally accepted
experimental technique for the characterization of the failure of
concrete under high strain rate deformation. A systematic and
extensive investigation of concrete at high speed loading conditions
is indispensible for the modeling of its mechanical response in order
to furnish engineers a useful and dependable criterion for structural
design.

Many of the experiments carried out on dynamic strength of
concrete, as well as some on rock, have been reviewed in a previous
work [25]. Table 3-1 gives a summary of some studies on unconfined
concrete tests. It has been found that most of the studies used
different testing equipments, and conclusions were based on the
fracture strengths.

To examine every aspect of concrete behavior under dynamic
compressive testing is only possible by carrying out a complete
progressive failure analysis of a test specimen. The split Hopkinson

 44

Table 3-1. Summary of previous studies on unconfined dynamic concrete properties.

DYNAMIC UNCONFINED CONCRETE TESTS	McHenry, D. & Shideler, J. J. (review paper) [26]	Watstein, D. [33]
DATE	1956	1953
EQUIPMENT OR TEST METHOD		Cushioned impact & drop hammer
SPECIMEN		3x6" cylinder for dynamic test 6x12"cylinder for standard test
LOADING RATES	1-1000 psi/s	10^{-6} to 10 s^{-1}
CONCLUSIONS	a. In the range of loading ranges of 1 to 1000 psi/s, the compressive strength is a direct function of the rate of loading. b. At loading rate of 1000 psi/s, the strength is 109% of the "standard tests" (20 -50 psi/s) c. At least 50% of the ultimate load can be applied at any rate without affecting the strength.	a. Secant modulus of elasticity, energy absorption and strain to failure all affected by loading rates. b. The maximum ratio of dynamic to static compressive strength was about 1.8 for strain rate of 10 s-1. c. The values of the secant moduli of elasticity increased significantly with the rate of loading. d. The average observed ratio of the dynamic to static energy ranged from about 0.9 to 2.2 for the range of loading rates used.

Table 3-1. continued.

DYNAMIC UNCONFINED CONCRETE TESTS	Goldsmith, W. and et al. [15]	Bhargava, J. and Rehnstrom, A. [3]
DATE	1966	1977
EQUIPMENT OR TEST METHOD	longitudinal wave propagation	SHPB: .1m dia. 2.0m long inc. and tra. bars, 0.25m striker
SPECIMEN	0.75x24"rod	0.1x0.2m cylinder
LOADING RATES		N.A.
CONCLUSIONS	a. The dynamic Young's modulus of concrete is significantly greater than its corresponding static value. b. The wave propagation process appeared to occur without dispersion and relatively little attenuation, indicating that the material could be represented on a macroscopic scale as an "elastic" substance with a small structural damping coefficient.	a. The dynamic strength of concrete obtained was 40-45% higher than the static strength.

Table 3-1. continued.

DYNAMIC UNCONFINED CONCRETE TESTS	Graham, D. E. [16]
DATE	1986
EQUIPMENT OR TEST METHOD	MTS
SPECIMEN	6x12" cylinder
LOADING RATES	10^{-5} to 10^{-2} s^{-1}
CONCLUSIONS	a. Under dynamic conditions the compressive strength at age 90 days is increased by 18 to 23 %, the elastic modulus is increased by approximately 3 to 7%, and Poisson ratio is increased by about 5 to 15%.

pressure bar system studied in the previous chapter appears to be the best available apparatus to provide a large amount of information on a dynamic compressive testing specimen. With this system a series of experiments on unconfined concrete specimens were performed cooperatively by the concrete research group in the Department of Aerospace Engineering, Mechanics, and Engineering Science at the University of Florida. The wave reconstruction technique presented in the previous chapter was also employed in the calculation of tested results. Based on this, explanations will be proposed for the failure process in these tests.

3.2 Experiments and Calculations

Concrete specimens tested in this experiment were prepared at the U.S. Army Waterways Experiment Station (WES), where concrete cylinders were cast in PVC pipe molds of 76.2 mm diameter and cut to length after cure. The aggregate used was limestone with the maximum size of 9.53 mm. Table 3-2 lists the mix of these specimens. All tested specimens were ground at the University of Florida to ensure the parallelism and smoothness of end faces.

Eleven nominal 76.2 mm long specimens were tested with two surface strain gages (Micro-Measurement CEA-06-500UW-350) mounted midway between their ends, one measuring axial strain ϵ_z and one measuring lateral (hoop) strain ϵ_θ. One specimen (w26) was tested with both strain gages laterally mounted on its surface. Another thirteen nominal 76.2 mm long and nine 33.02 mm long specimens were tested with no surface strain gages. The firing chamber nitrogen pressures of

these tests were controlled and almost evenly expanded between 1.24 MPa and 4.14 MPa with an aim to obtain well-distributed impact speeds.

Two channels of the Nicolet oscilloscope were employed to record the incident and reflected pulses (input from gage station on the incident bar), and the transmitted pulse (input from transmitter bar gage station). For gaged specimens, in addition to these three pulses two more pulses from axial and lateral gages on the specimens were recorded with the other two channels in the Nicolet oscilloscope.

Velocity-time, stress-time, strain-time, and strain rate-time curves of each specimen were calculated from dispersion corrected incident, reflected, and transmitted pulses employing equations in section 3.2 of chapter 2. The ratio of lateral strains (measured from gaged specimens) to axial strains (calculated from the SHPB results) was determined for each specimen with strain gages.

Table 3-2. Mix of concrete specimens.

```
Water/Cement Ratio (based on total cementitious
    material)  ·····························  0.27
Type I Portland Cement  ····················  385.9 kg
Silica Fume  ······························  68.1 kg
Fine Aggregate (manufactured limestone
    from Vulcan Materials, Calera, Ala.) ····  844.4 kg
Coarse Aggregate (manufactured limestone
    maximum size 9.53 mm) ················  457.6 kg
Water ·····································  122.6 kg
High Range Water Reducing Add Mixture ······  9.1 kg
DAXAD-19-2% by weight of cementitious material
    (superplasticizer). Prepared by Concrete
    Technology Division, WES.
One cubic yard with slump 215.9 mm.
```

3.3 Results

Experimental results are representatively given in Figures 3-1 through 3-13. Pulses recorded from the SHPB and axial as well as lateral strains from surface strain gages of two specimens (w20, w44) are shown in Figure 3-1. Figures 3-2,3,4,5 show the velocities versus times curves at both the first and second bar-specimen interface of four nominal 76.2-mm-long specimens and four 33.02-mm-long specimens. For the same two groups of four specimens each, stress-time curves at interfaces and stress (average), strain, and strain-rate versus time curves are given in Figures 3-6,7,8,9, and in 3-10,11,12,13 respectively. Figure 3-14 are axial strains (solid) and lateral strains (dashed) versus time offset plots for eleven 76.2 mm-long specimens, which had axial and lateral strain gages mounted on the surface, and the two lateral strain gage readings of specimen w26 (Fig. 3-14), which had both strain gages laterally mounted. Figure 3-15 compares axial strains recorded from the SHPB (solid line) to the measured strains (dashed line) from strain gages on the specimen surfaces for two gaged specimens. Stress-axial strain (solid line) and lateral strain versus axial strain (dashed line) curves of twelve gaged specimens are given in Figure 3-16.

Table 3-3 presents experimental data for all 76.2 mm and 33.02 mm specimens. The first column of this table gives the specimen identifications. Specimen I.D.s with initial letter "w" are nominal 76.2-mm-long specimens. The rest are short specimens (33.02 mm nominally). Letter "G" next to specimen I.D. marks gaged specimens. The results
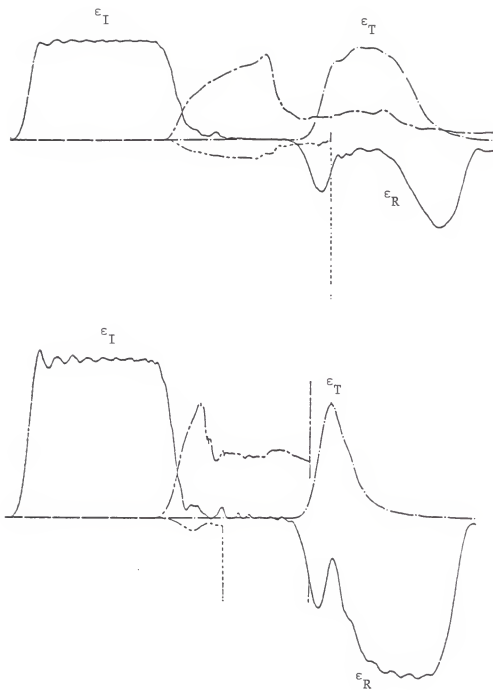
Figure 3-1.   Strain pulses in pressure bars and axial and lateral
specimen surface strains for w02 (upper) and w44.
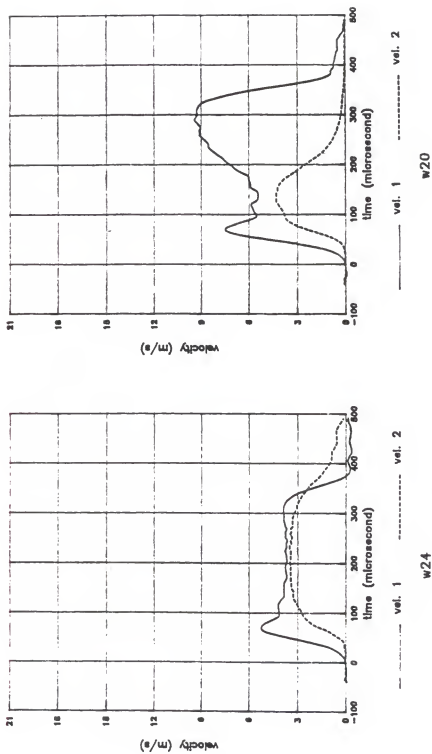
Figure 3-2. Velocity-time curves at interfaces of long specimens w24 and w20.
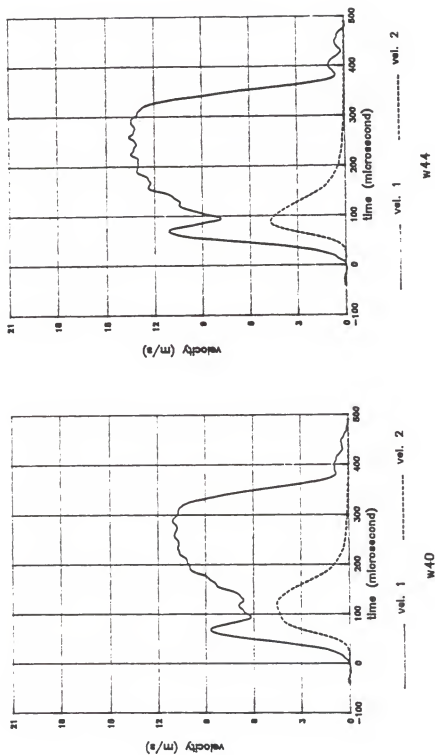
Figure 3-3.   Velocity-time curves at interfaces of long specimens w40 and w44.
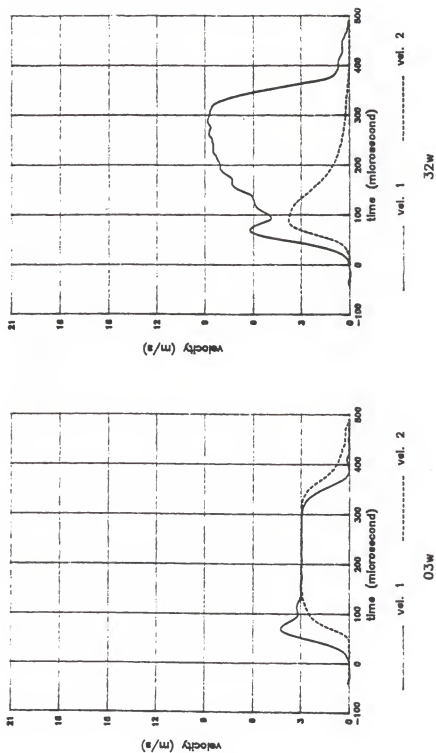
Figure 3-4. Velocity-time curves at interfaces of short specimens 03w and 32w.
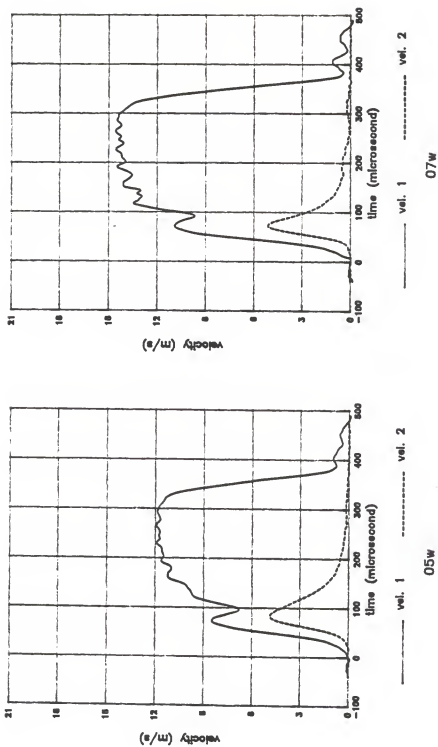
Figure 3-5.   Velocity-time curves at interfaces of short
specimens 05w and 07w.
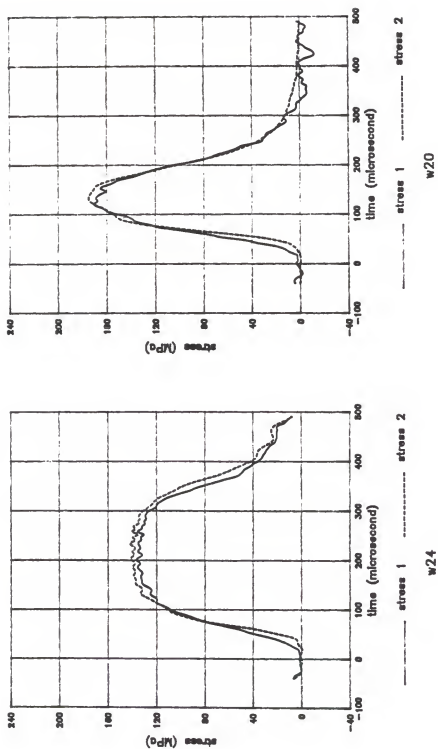
Figure 3-6. Stress-time curves at interfaces of long specimens w24 and w20 .
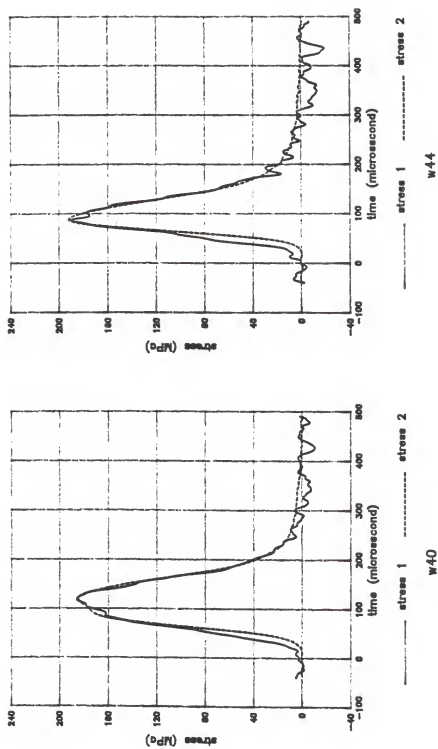
Figure 3-7. Stress-time curves at interfaces of long specimens w40 and w44.
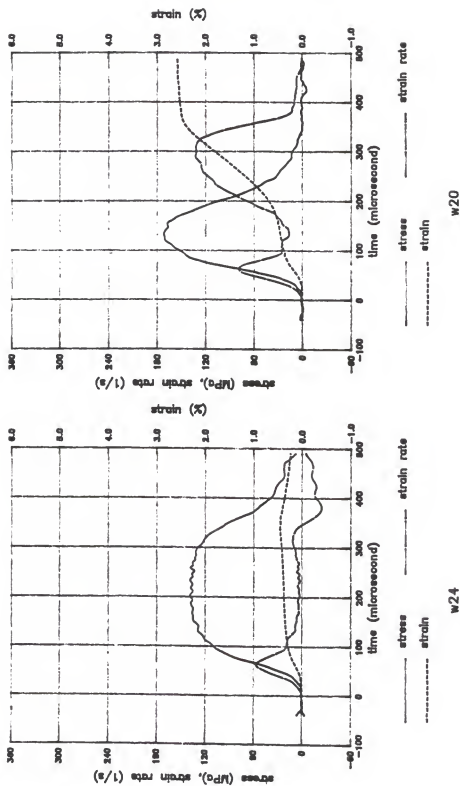
Figure 3-8. Average stress, strain rate, and strain versus time curves of long specimens w24 and w20.
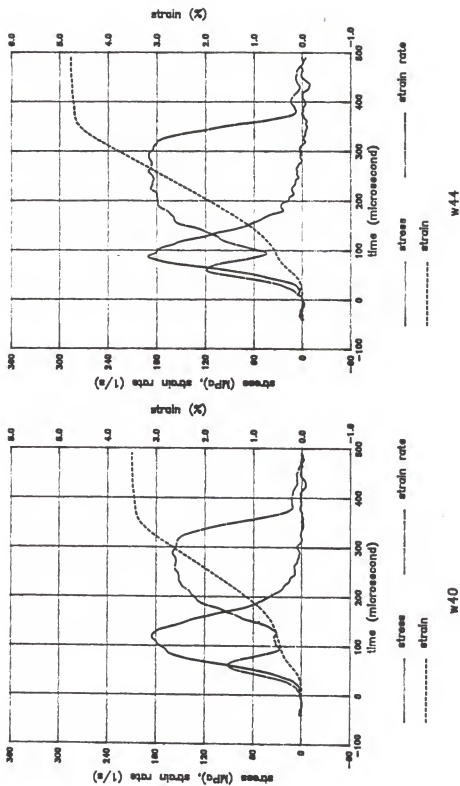
Figure 3-9. Average stress, strain rate, and strain versus time curves of long specimens w40 and w44.

59
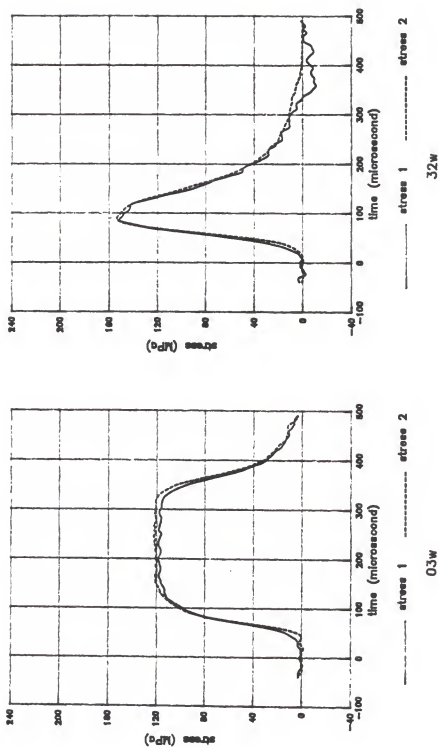
Figure 3-10. Stress-time curves at interfaces of short specimens 03w and 32w.
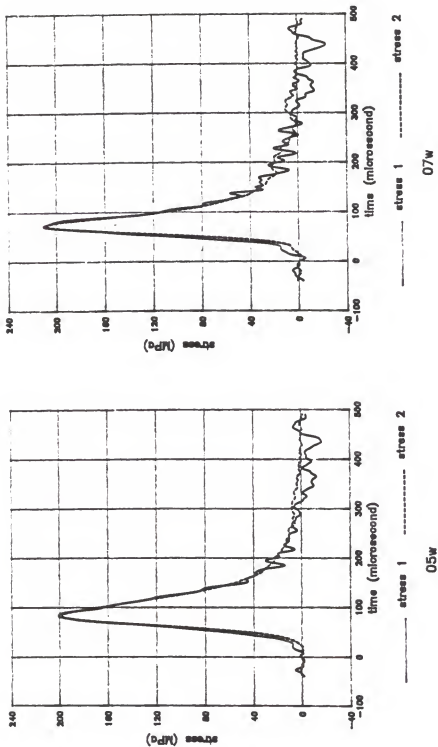
Figure 3-11. Stress-time curves at interfaces of short
specimens 05w and 07w.
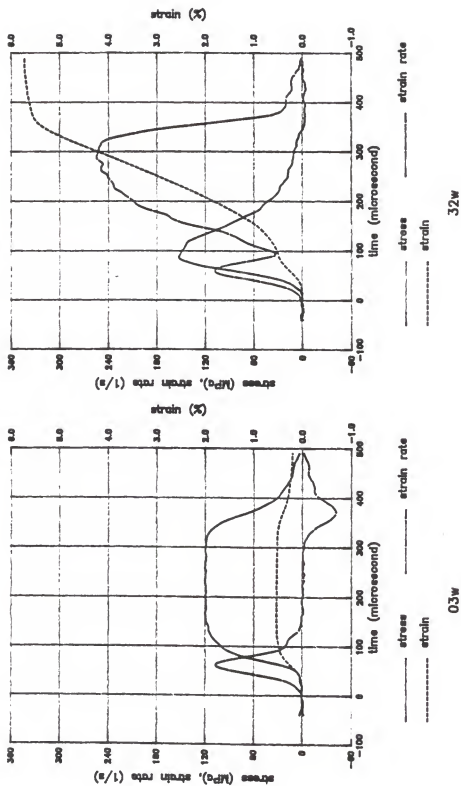
Figure 3-12. Average stress, strain rate, and strain versus time curves of short specimens 03w and 32w.
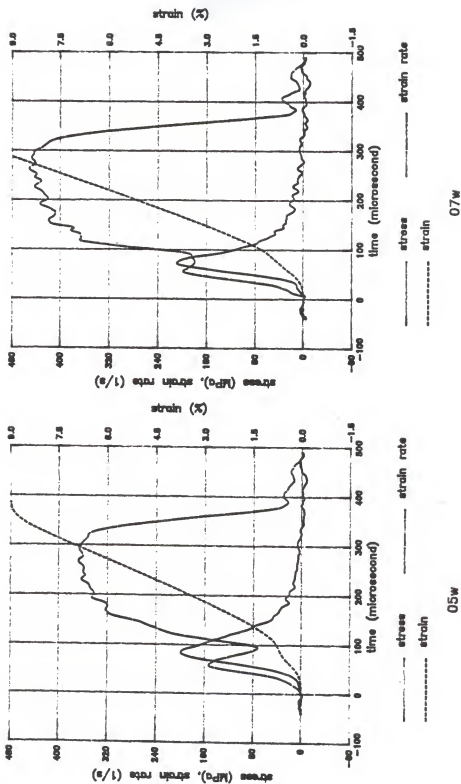
Figure 3-13. Average stress, strain rate, and strain versus time curves of short specimens 05w and 07w.
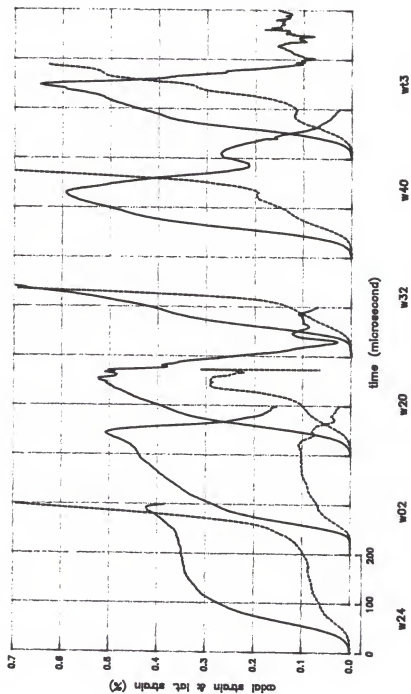
Figure 3-14. Axial (solid curves) and lateral strains (dashed curves) versus time of long specimens with surface strain gages.

64
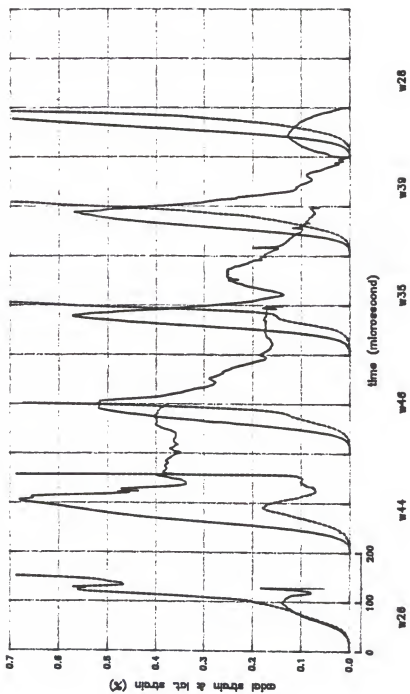
Figure 3-14. continued.
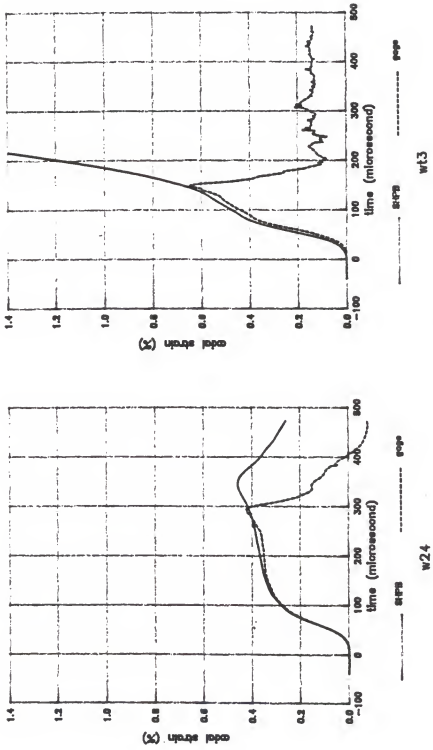
Figure 3-15. Axial strains from surface strain gages and the SHPB respectively of two long specimens w24 and wt3.

66
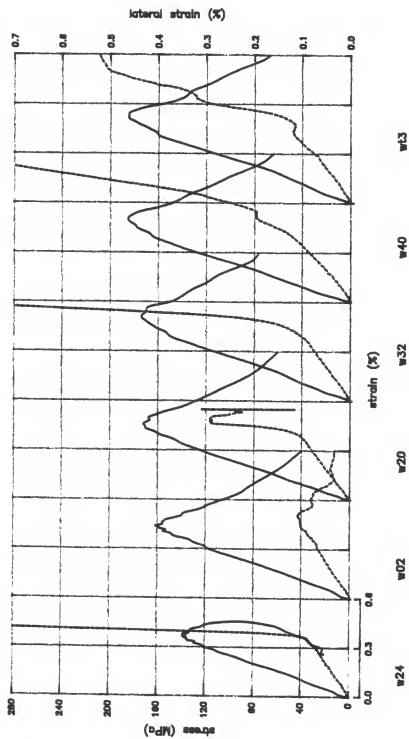
Figure 3-16. Stress-axial strain (solid) and lateral strain-axial strain (dashed) curves of gaged long specimens.
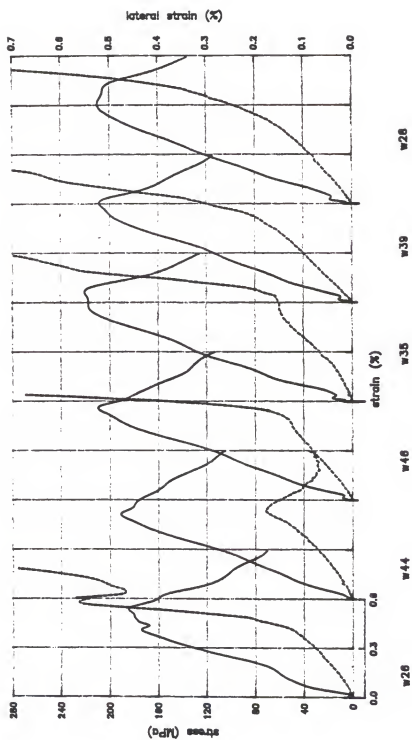
Figure 3-16. continued.

Table 3-3. Results of tested concrete specimens from WES.

SPECIMEN I.D.	IMPACT VEL. (m/s)	TIME (μs)	MAX. STRESS (MPa)	STRAIN (%)	STRAIN RATE (1/s)
W03	6.59	201.5	132.5	.331	1.3
W24	6.97	201.5	138.8	.367	3.0
W10	7.72	164.0	144.1	.417	9.5
W42	8.13	156.5	153.5	.415	11.3
WO2 G	8.38	169.0	161.4	.439	9.3
W43	9.49	126.0	165.0	.433	24.0
W20 G	9.61	133.0	171.9	.456	16.2
W21	9.87	132.5	177.2	.445	16.9
W08	10.14	130.5	180.2	.483	20.8
W36	10.79	119.5	181.3	.52	32.5
W32 G	10.84	119.5	173.8	.508	37.5
W40 G	11.0	118.5	185.2	.499	34.1
W09	11.39	116.0	180.0	.536	43.2
WT3 G	11.41	112.5	186.4	.519	35.4
W26 G	11.89	115.5	184.7	.537	48.0
W11	12.49	104.0	173.6	.565	47.4
W44 G	13.45	87.0	191.0	.515	55.9
W15	13.82	87.5	204.9	.519	61.3
W46 G	14.85	89.5	209.5	.56	72.8
W19	14.79	89.0	217.3	.567	70.5
W39 G	15.73	88.5	208.2	.605	85.6
W37	15.88	81.5	204.7	.598	98.8
W30	16.90	80.5	203.3	.576	121.5
W35 G	17.34	86.5	220.4	.667	99.3
W28 G	17.51	76.0	209.7	.608	137.9
03w	5.87	167.0	119.7	.534	0.0
32w	8.99	86.5	152.5	.476	42.4
31w	8.99	90.0	152.4	.488	43.4
05w	11.91	83.5	199.3	.639	93.0
01w	12.85	82.5	208.3	.613	103.4
06w	13.19	80.0	209.3	.722	129.2
07w	14.46	72.5	209.0	.749	179.9
08w	15.36	72.0	233.9	.696	181.8
02w	17.12	66.5	241.7	.752	223.0

given are impact velocities (I. VEL.), times at which maximum stresses were picked (TIME), maximum stress (MAX. STRESS), strain at maximum stress (STRAIN), strain rate at maximum stress (STRAIN RATE).

Figure 3-17 shows points of the maximum stresses versus the strain rates at the associated maximum stress for all 34 specimens. A semilog curve of the form

$$\sigma = A + B \ \ln(\ \dot\epsilon/\dot\epsilon_0)$$

with $\dot\epsilon_0 = 1.0 \ s^{-1}$, A = 109.8 MPa, and B = 20.6 MPa, is plotted along with test points in Figure 3-17. The constants A and B were determined by least square curve fitting.

3.4 Discussion

From Figures 3-2,3,4,5, where the variations of velocities at the specimen-bar interfaces versus time were plotted for specimens with same mixtures but two different nominal length (76.2 mm and 33.02 mm), details of dynamic uniaxial compressive tests can be drawn.

For specimen 03w (Figure 3-4), which had no apparent damage during the test, the second interface velocity (vel.2) rose at about 50 microseconds after the first interface velocity (vel.1), which is a little longer than the counterpart of damaged specimens. Before approximately 140 microseconds, at which the two velocities almost coincide, the specimen experienced compressive deformation. Total specimen deformation in this period can be represented by the area between the two interface velocities. From 140 microseconds to 300 microseconds the specimen traveled along with the whole system at approximately 3 meters/sec, and no further deformation took place
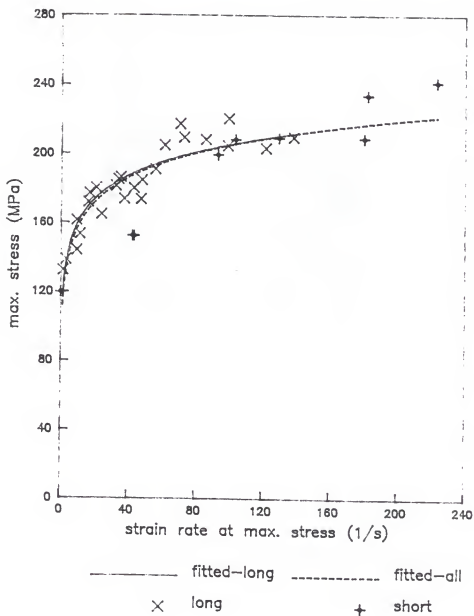
Figure 3-17. Maximum stress versus strain rate at maximum stress for WES concrete specimens and fitted semi-logarithmic curve of both long and short specimens.

during this period. At 300 microseconds the measured velocities diverged and the specimen elongated in the axial direction or lost contact with the bars.

If there is no permanent deformation in the specimen, the two enclosed areas between the two velocities should be identical. However, gaps exist in the interfaces, which are difficult to avoid for all kinds of compressive tests, giving pseudo deformation and contribute to apparent total measured deformation. This shortcoming has been reduced by pushing the incident bar, specimen, and the transmitter bar against the shock-absorbing spring in the SHPB experiments. That induces a slight initial loading force on the specimen, but this load is insignificant in comparison to the impact test loads. If results are drawn for all specimens tested under similar conditions, the effects from interface gaps would be minimized. Another source of pseudo deformation may come from gaps that open due to the end of the loading period.

For specimens which were damaged during the test the interface velocities also reveal information that relates to the progress of deformation and fracture. In Figure 3-2 the velocity plots of specimen w24 show the rapidly deformed period ($0\mu s$ - $100\mu s$), the approximate constant deformation rate period ($100\mu s$ - $270\mu s$), where vel.1 and vel.2 maintained almost constant difference, and the fracture period ($270\mu s$ - $310\mu s$), where vel.1 increased while vel.2 dropped. In the second period (approximately constant deformation rate period) there exists a peak at about $200\mu s$ in the second interface velocity. Prior to this peak the 2nd interface velocity was

continually increasing, and it decreased after this peak. The total deformation in this period, which is also shown in Fig. 3-8, is relatively small if it is compared to that of the first period.

The lengths of these three periods and the beginning times of the second and the third period change with the increase of impact velocity. With higher impact velocity the constant deformation rate period approaches a point in the time scale used. The time at which this peak happened moves ahead earlier for higher velocity impact tests, and it is before that of the dip of the vel.1 in some tests. This means that the vel.2 declined suddenly before the vel.1 abruptly increased. The specimen experienced a very high rate of deformation and may have been pulverized in the third period.

The size of the specimen affects the three deformation stages in a way that short specimens behave like long specimens with much higher impact velocities. However, the resulting curve-fitted plots (Figure 3-17) of maximum stresses versus the corresponding strain rates of all specimens (dashed line) and that of long specimens alone (solid line) show little difference. In the present experiment the shorter specimen size contributes to higher strain rates, higher maximum stresses, and a comparatively closer match of stresses at the two specimen-bar interfaces.

The closeness of stresses at the two interfaces indicates that the specimen has a uniform loading state along the length, which is critically important for the SHPB test. For the current study the uniform loading state was pretty much satisfied after $\approx 60 \mu s$ of the rise period (Figures 3-6,7,10,11).

Because of the innate inhomogeneity and anisotropy of concrete, as well as the pre-existing cracks in the boundaries of aggregates and matrix, it had been suspected that the surface strain gages only presented local information. The good agreement with the SHPB axial strains indicates that this was not so in these tests. The strain gages mounted on the surface of specimens have provided valuable information for the analysis of deformation and fracture processes of the present SHPB tests. If strain gages function normally before the concrete specimen splits into pieces, the readings from these strain gages could be considered representing the global behavior of the test specimen.

All available surface strain gage readings were presented in Fig. 3-14. In Fig. 3-14 (cont.) the two lateral strain readings from laterally mounted surface strain gages on specimen w26 show that the gage measurements are repeatable and are very reliable to a certain stage. The close agreement of axial strains measured respectively from the SHPB, which represent global behavior of the tested specimens, and the mounted gages, which give local response of the tested specimens, shown in Figure 3-15 again demonstrates the reproducibility of gage strain readings. Through careful examination it is possible to find out that these strain gage readings possess similar patterns. These patterns are helpful in figuring out the fracture processes involved in the SHPB tests.

By examining the lateral strain reading of specimen w24 (Fig. 3-14), it is found that three stages of lateral deformation are involved. In the first stage, which includes the incipience of

lateral deformation and a steep rising part, the specimen was rapidly deformed. The second stage, roughly from $100\mu s$ to $200\mu s$, is a more slowly increasing segment. The final stage consists of a suddenly ascending part and the specimen is believed fractured in this stage.

Each stage of the lateral deformation can correlate to an associated period in the interface velocity plots. The first stage seems correlated well to the rapidly deformed period. The earlier segment of the almost constant deformation rate period ($100\mu s$-$200\mu s$) in the interface velocity plots may associate with the 2nd stage of lateral deformation. And the later segment along with fracture period in the interface velocity plots are the counterpart of the 3rd stage of the interface velocity plots.

Not all lateral strain readings of gaged specimens are distinguishable into three stages as on w24. However, it seems that the first stage can always be found for every specimen. It has been observed that the 1st stages, like the first peak (at $\approx 70\mu s$) and the first dip (at $\approx 90\mu s$) of the vel.1 in interface velocity plots (Figs. 3-2,3,4,5), happened within $100\mu s$ regardless of impact velocities and specimen sizes. Also in axial strain curves (Figs. 3-8,9,12,13) an inflection area occurred around $90\mu s$ for all tested specimens. It is believed that the incident pulse rise time periods ($\approx 65\mu s$) are the origin of these phenomena. From the above discussion it can be concluded that the pulse amplitude and rise time of the incident pulse play a key role in the SHPB test.

For the present experiment the load increasing rates of the incident pulse, which are calculated from the average amplitude and

pulse rise time (≈65μs), range from 2 MPa/μs to 5 MPa/μs. And the stress increasing rates in the specimen, which are obtained by dividing the maximum stress by the time at which the stress reaches its maximum, are between 0.6 MPa/μs and 4.0 MPa/μs. There are two ways to control the load increasing rates of the SHPB test. One of these, which has been used in almost all the SHPB systems, is through the rise of the impact velocity to increase the load increasing rate. This method, however, at the same time alters load amplitudes. The other method is to control the incident pulse rise time without changing the impact velocity or the pulse amplitude. This can be achieved by cushioning or by changing the striker bar's impact end shape.

The change of load increasing rate, i.e. the changes of the amplitude of the incident pulse in the present tests, in turn, changes strain rate-time and the strain-time curves of a test specimen. However, there is no period where the specimen experienced constant strain rate loading, if it is considered from the strain rate-time curve. If the strain-time curve is taken into consideration, a constantly increasing period can be approximately specified. This period is picked from roughly after the incipience of the axial strain to the inflection area of the strain-time curve. From the earlier discussion, this period is primarily dependent on the load rise period of the incident pulse.

Although approximately flat valleys are observed in the strain rate-time curves of some of the present test results (eg. w24 and w20 in Fig. 3-8), those specimens may have been subjected to some degrees

of damage before these almost constant strain rate loading periods.
And the use of information within these periods to represent specimen
behavior at high strain rates may not be well justified. So, in the
SHPB test, if a constant strain rate loading condition is to be
fulfilled, only the results from the strain-constantly-increasing
period can be used in the characterization of strain-rate effects on
brittle specimens. Moreover, within this strain-constantly-increasing
period the stress uniformity in the specimen has to be fully
satisfied.

Figure 3-18 shows two interfacial stresses of a long specimen
(w39) and a short specimen (08w). They were subjected to almost the
same impact velocity (15.73 m/s and 15.36 m/s). It is apparent that
specimen w39 had experienced less equilibrium stress state in
comparison to its short counterpart, specimen 08w. To achieve stress
uniformity and at the same time to obtain maximum stress within the
strain-constantly increasing period, it is more suitable to use short
specimens (length/diameter≈0.5) along with the control of incident
pulse rise time.

In Lindholm et.al. [23] test results of Dresser Basalt, the
incident pulse increased from zero to ≈190 ksi (≈1300 MPa) in 26μs.
That yields a load increasing rate of 52 MPa/μs, which is 10 times
higher than the highest load increasing rate of the current
experiment. With such a high loading rate, it is difficult to achieve
a uniform stress field across the specimen. Non-uniform loading and
inertia may dominate in the fracturing process of specimens in their
tests. Hence, the effects of strain-rate are very difficult to be
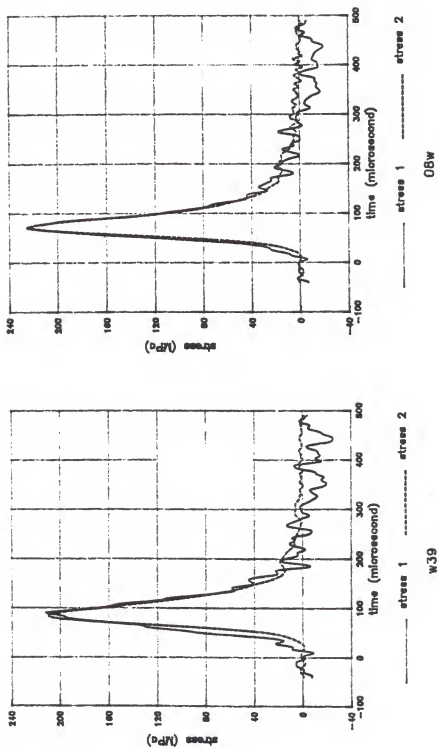
Figure 3-18. Stress-time curves at the two interfaces of long specimen w39 and short specimen 08w.

extracted from such high loading rate SHPB test results. And this led to their uncertainty in the interpretation of fracture stress data for brittle materials tested with the split Hopkinson pressure bars.

Much higher loading rates have been used in a number studies for the dynamic response of rocks [14,35] using SHPB configurations. Conclusions made from those investigations may have been misled by the test results with no insurance of stress equilibrium across the specimens.

In the SHPB tests, the load increasing rate (rise period of the incident pulse), the magnitude of the applied load (average pulse amplitude) as well as the duration of the constant loading period (incident pulse duration) are the three major factors that determine the damage patterns of the brittle specimens. These three factors are determined from the configuration of the incident pulse and in turn depend on the system's configuration of the SHPB.

For all specimens tested there are three damage patterns that can be sorted out. Specimen w03 and 03w both belong to the first category. Those two specimens were not damaged in the test. They experienced lower loading rates and lower magnitudes of load but longer constant load duration in comparison to the other specimens. The loading rates and applied load magnitudes were not high enough to initiate cracks which are large and dense enough to coalesce and fracture the specimens during the constant loading period. Although during the constant loading period no deformation took place at all, had the constant loading period been longer the two specimens might have been further deformed and split or fractured.

The second category includes specimens like w24, w02, w40, and etc.. The loading rates and load magnitudes of this category were higher than those of the first category. During the load increasing period the specimens in this category, it is believed, had experienced cracking in varied degree of severity. The higher the loading rates and the load magnitudes, the more severe were the cracks and the shorter the constant load duration they were able to sustain. Further increase of loading rate and load magnitude would carry this category into the third category.

So, in the tests of brittle materials with the SHPB, if the specimen does not have major cracks in the load increasing period, which would coalesce during the duration of the constant loading period, whether the specimen is eventually damaged would depend on the duration of constant loading period. For a long enough loading pulse, the number and the size of cracks would increase during the constant loading period and finally the cracks merge together and fracture the specimen.

If the specimen already has developed some major cracks in the load increasing period, these major cracks would join and fracture the specimen during the constant loading period. The time required to fracture the specimen in the constant loading period depends on those cracks which had existed and developed prior to and during the load increasing period and in turn depends on the load increasing rate and the magnitude of the applied load. This time period can be observed in the stress-time plots, which is termed as "duration of waiting time," and the failure type is termed as "delayed failure" in [25].

In the third category the constant load period shrinks to zero and the specimen fractured within the load increasing period. Specimens belonging to this category were damaged under approximately constant strain rate loading conditions, if strain rates are measured from the slope of constantly increasing period in their strain-time plots. As long as the stress equilibrium requirement in the specimen is ensured, the results from this category are more suitable for the characterization of the strain-rate dependence of the response of brittle materials than from the category where failure is delayed.

3.5 Conclusions and Recommendations

An extensive series of dynamic experiments was carried out on high strength concrete specimens with the split Hopkinson pressure bar. Wave dispersion correction techniques were employed and gave more accurate results.

In the SHPB test, the incident pulse contains three parameters. They are pulse rise time, pulse amplitude, and pulse duration. For the tests of brittle materials, in order to vary the strain rates, more information may be obtainable by changing the pulse rise time and keeping the pulse amplitude constant. An essential requirement that has to be fulfilled in the test is that within the specimen the stresses in the longitudinal direction should be uniform. With the interface stresses it was able to check if this requirement is assured. Specimens with length to diameter ratios equal approximately to 0.5 gave better results in achieving the uniform stress condition.

In the present tests, different strain rates were only obtained

by the change of the incident pulse amplitude. Specimens which had higher impact velocities fractured within the incident pulse rise period and also were subjected to approximately uniform loading state. These specimens showed higher maximum stresses than the failure strength of statically tested specimens. Those specimens with delayed failures had not fractured in the pulse rise period, but the stresses they experienced at that period are also higher than the static failure strength. It can be concluded that dynamic failure strengths are higher than static failure strengths for the concrete tested.

The SHPB is the only apparatus currently existing that can be employed to portray so much detail of a dynamic material testing. With the use of specimen surface strain gages more information was obtained. These strain gage results proved very helpful in the understanding of the failure processes of the specimen tested. If a high speed camera could be used in addition, a more complete picture of the progress of dynamic fracture would be obtained, which would be very valuable.

CHAPTER 4
AXIAL DYNAMIC COMPRESSIVE STRENGTH OF PASSIVELY
CONFINED CONCRETE

4.1 Tests of Slurry Infiltrated Fiber Concrete (SIFCON)

4.1.1 Introduction

The intrinsically brittle type of failure which occurs under tensile stress systems or impact loading has been a notorious problem for cementitious materials. Attempts to toughen cement-based materials have led to the employment of fibers to reinforce concrete. However, the workability and compaction problems set barriers to achieve the required toughness of the otherwise brittle materials. It has been shown that the ultimate mechanical properties of a steel fiber-reinforced concrete composite depend on the fiber volume fraction, fiber aspect ratio, fiber/matrix bonding properties, and fiber orientation and distribution in the matrix. Study also showed that the increase of some parameters mentioned, such as fiber volume fraction, would increase the ultimate strength, flexural toughness, and energy absorbing capacity of the fiber reinforced concrete.[17]

Slurry infiltrated fiber concrete (SIFCON) made by a non-conventional technique developed by Lankard Materials Laboratory (LML) has demonstrated much higher steel fiber volume fraction (up to 18%) than those made by conventional mixing of concrete constituents and steel fibers, which achieve only 2.0 volume percent in fiber content.

82

Uniaxial static compression and flexural tests conducted by LML have shown the superior mechanical properties of SIFCON to the plain, conventional concrete and the conventional steel fiber reinforced concrete respectively. Some other experiments including an impact resistance test recommended by ACI Committee 544 were also carried out at LML [22]. The impact test, made by dropping a 4.54 kg soil compaction hammer 0.457 meter onto a hardened steel ball placed in the center of the castable specimen, however, measured only the number of blows required to crush the material, as well as the number of blows to fully separate the cracked pieces.

In the characterization of impact properties, it is desirable to determine the stress-strain response of concrete at varying strain rates. And further correlations of some of the mechanical properties with the strain-rate effects would facilitate the understanding of material behavior under impact loads. In this section the SHPB was employed to test SIFCON specimens. Attempts were made to find out the complete stress-strain curves and the failure mechanisms of SIFCON at high strain rates.

4.1.2 Experiments and Results

Two batches, with six and ten specimens respectively, of SIFCON specimens tested in this study were obtained from New Mexico Engineering Research Institute, University of New Mexico. The slurry used and steel fiber type, fiber aspect ratio, and fiber volume fraction for the reinforcement were not available. A total of sixteen specimens nominally 76.2 mm in diameter and 63.5 mm long were ground

at the University of Florida to ensure the parallelism and smoothness of end faces.

The first specimen (fe) tested under an impact velocity of 10.52 m/s was apparently not damaged. Six subsequent tests were conducted on the same specimen and with the same impact velocity intending to see if it would be finally damaged. Permanent deformation in the axial direction was measured after the last test. Higher impact velocities, ranging from 11.68 m/s to 18.21 m/s, were employed in the tests of the other fifteen specimens. The permanent deformations were measured for each tested specimen. They were then divided by the specimen original length and converted to permanent strain in percentage. Table 4-1 shows, for all the specimens tested, the impact velocity, the original specimen length, and the permanent deformation strain in percent.

Figure 4-1 gives raw pulses recorded from the Nicolet scope for two specimens. Both of them had surface strain gages mounted in the lengthwise and circumferential direction. Dispersion correction techniques were applied in all test results. Figures 4-2,3,4 show the specimen-bar interface velocities of part of the first and the second batch specimens. In Figure 4-2 interface velocities of the first test and the fifth subsequent test performed on specimen fe were given. For the same specimens presented in Figures 4-2,3,4 the interface stresses and stress (average), strain rate, and strain versus time plots are presented in Figures 4-5,6,7 and 4-8,9,10. Stress-strain curves of six tests of five specimens of the first batch and six specimens of the second batch are shown in Figures 4-11,12.

Table 4-1. Permanent deformation of SIFCON tests.

SPECIMEN I.D.	IMPACT VELOCITY (m/s)	INITINAL LENGTH (meter)	DEFORMATION (%)
fe	10.52	0.062	1.97*
fb1	11.68	0.062	1.63
fd1	12.95	0.058	1.78
fa1	14.04	0.061	2.93
ff1	15.20	0.056	3.01
fc1	16.31	0.060	3.34
f2j	12.69	0.065	1.25
f2d	12.83	0.066	0.96
f2i	14.61	0.065	1.69
f2e	14.84	0.063	1.96
f2h	16.41	0.068	2.24
f2f	16.50	0.067	2.31
f2b	16.88	0.063	2.52
f2g	17.63	0.066	2.65
f2k	18.07	0.065	2.54
f21	18.21	0.062	4.47

* Deformation measured after the seventh test.
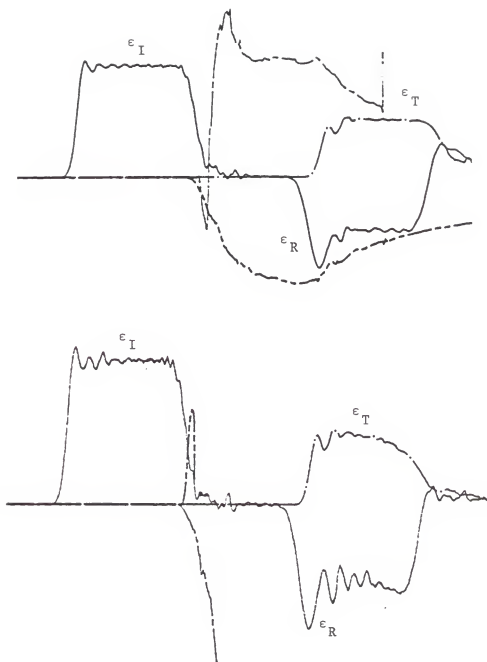
Figure 4-1. Strain pulses in pressure bars of specimen fbl (upper) and ffl.
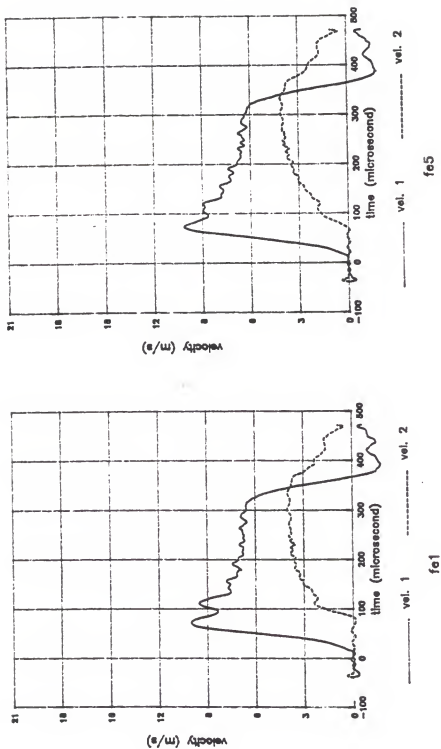
Figure 4-2. Specimen-bar interface velocities of the first and the fifth tests of specimen fel.
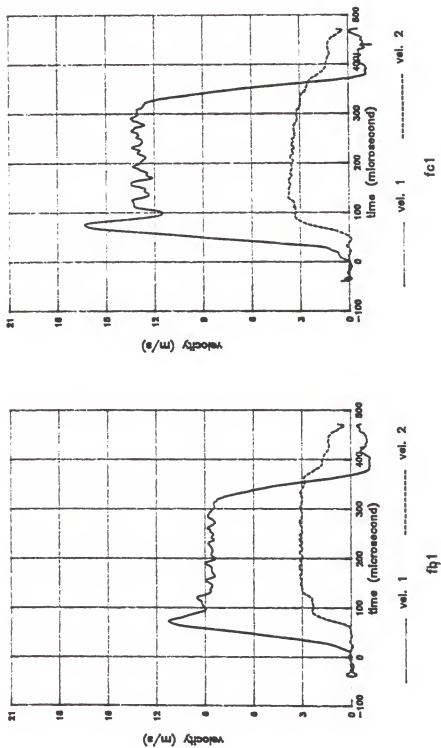
Figure 4-3.   Specimen-bar interface velocities of fb1 and fc1.
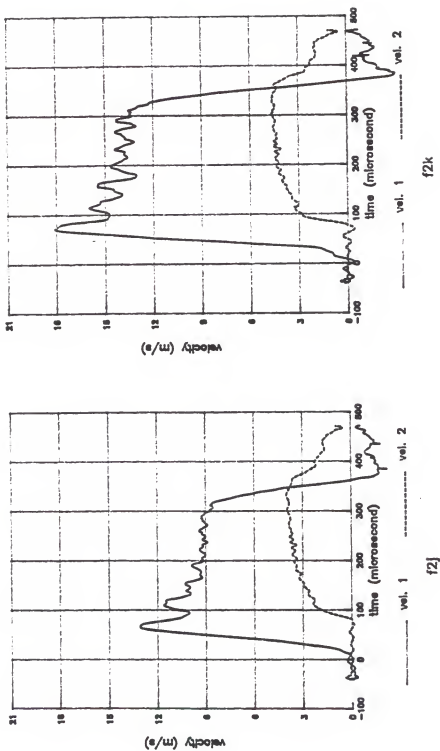
Figure 4-4. Specimen-bar interface velocities of f2j and f2k.
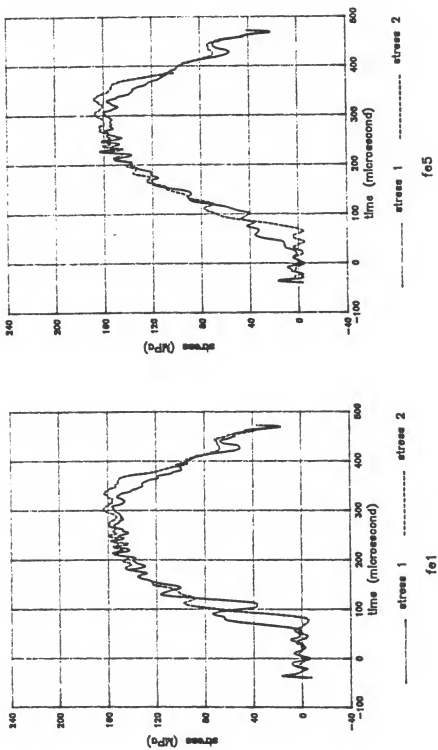
Figure 4-5. Specimen-bar interface stresses of the first and the fifth tests of specimen fe1.
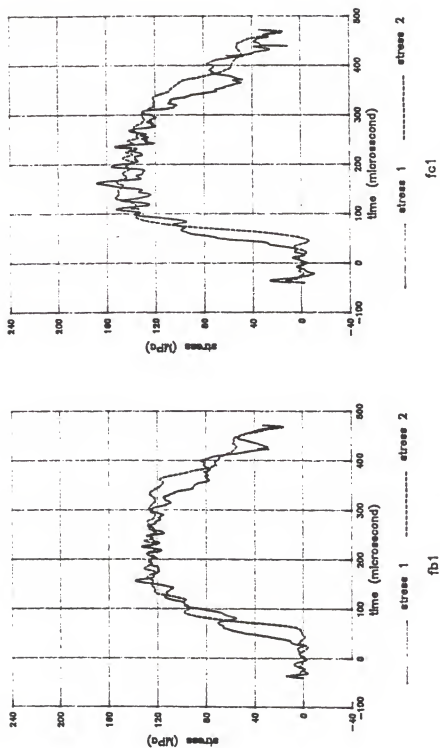
Figure 4-6. Specimen-bar interface stresses of specimens fb1 and fc1.
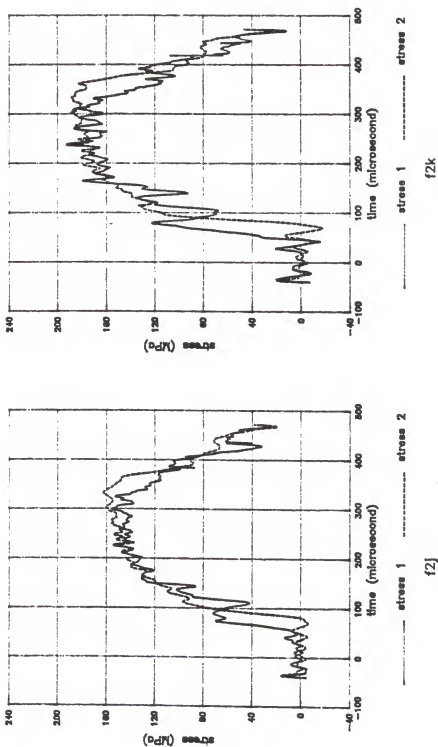
Figure 4-7, Specimen-bar interface stresses of specimens f2j and f2k.
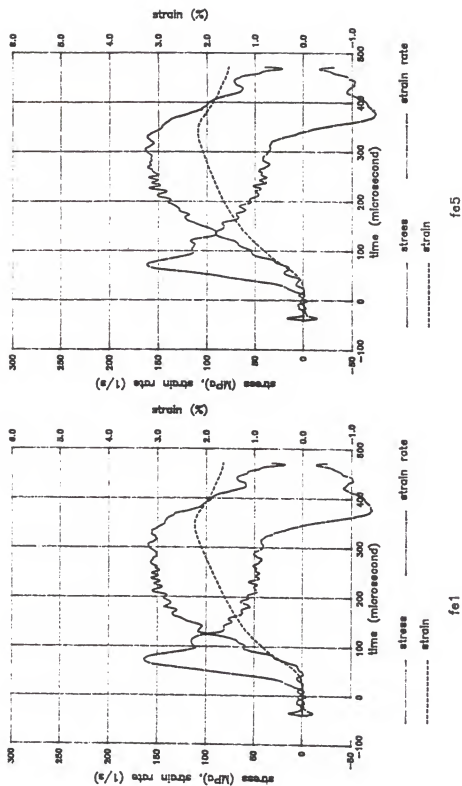
Figure 4-8. Stress (average), strain rate, and strain versus time of the first and the fifth tests of fe.

94
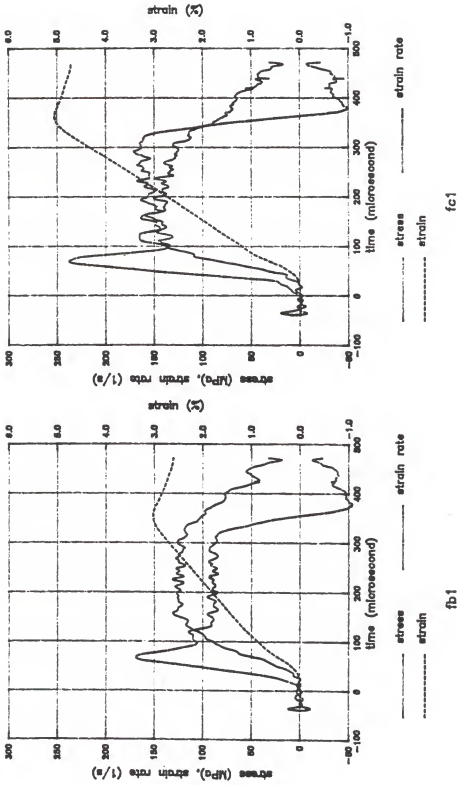
Figure 4-9.   Stress (average), strain rate, and strain
versus time of fb1 and fc1.
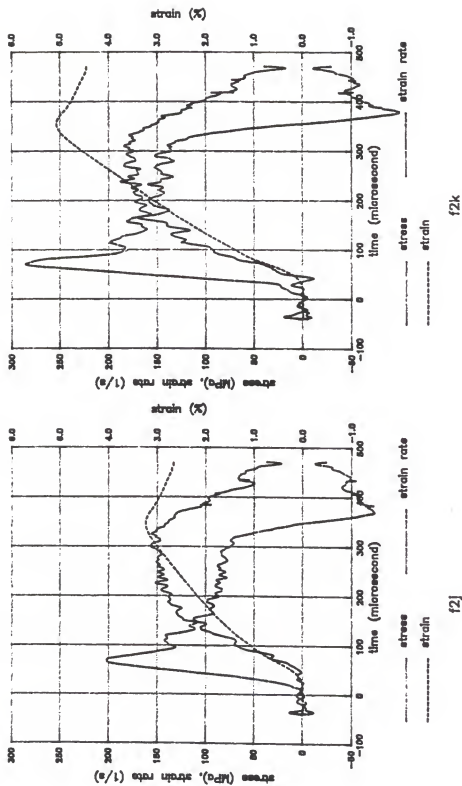
Figure 4-10. Stress (average), strain rate, and strain versus time of f2j and f2k.
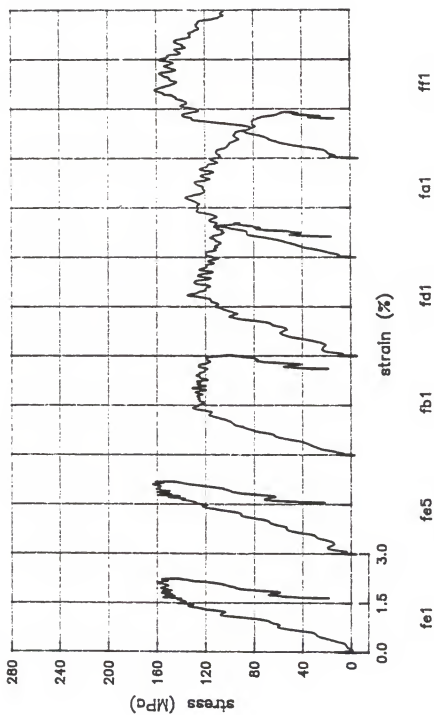
Figure 4-11. Stress-strain curves of the first batch SIFCON specimens.
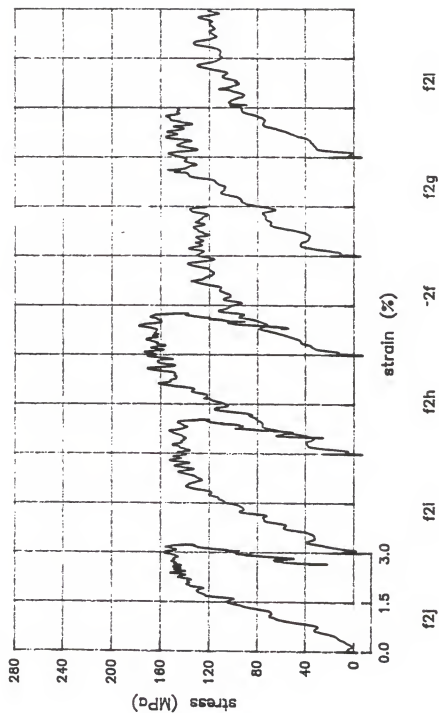
Figure 4-12. Stress-strain curves of the second batch SIFCON specimens.

4.1.3 Discussion

Because of the asperity of the circumferential surface of SIFCON specimens, the surface strain gage results are considered not suitable in portraying the global behavior. Figure 4-1 showed the peculiar strain readings. No surface strain gage reading is used in this study.

From Figure 4-1, it is found that the form of the reflected and the transmitted pulses is quite different from those of concrete specimens presented in the previous chapters. These pulse patterns distinguish the material systems. In Figures 4-2,3,4 the interface velocities plots show the progress of the impact test. The vel.2 rose much later as compared to that of WES specimens. It ranged from ≈50 μs to ≈85 μs, and is independent of the impact velocity. This says that it took longer for the pulse to transmit through SIFCON than through the WES specimens. There are two possible sources that account for the delayed incipience of vel.2. First, because of the steel fiber reinforcement, the end faces, although they were ground prior to the test, were considered not as smooth as the end faces of the WES specimens. The roughness of end faces may establish gaps that could not be reduced by simply pushing the incident bar, specimen, and the transmitter bar against the shock-absorbing spring, and thus prolonged the pulse transmit time. The second possibility comes from the inherent nature of the material system. It may take longer for a mechanical pulse to transmit a SIFCON specimen than a WES specimen.

The interface velocity plots also detail the deformation sequence of SIFCON under uniaxial compressive impact loads. All specimens were

subjected to very high-rate deformation in the beginning period. The lengths of this period are around 100 μs and are characterized by the rise segment of vel.2. After the first period, for some of the tested specimens the rate of deformation continuously decreased through the remainder of the entire loading period. For specimens fbl, f2e, f2f, and f2i the rate of deformation kept almost constant after the rise of the second interface velocity, and for specimens fdl, fal, ffl, and fcl a continually slow-increasing deformation rate is observed through the end of loading.

Among the first group, only the specimen fe had continually decreasing deformation rate following the rise of vel.2. Associated with the increase of the impact velocity, the rate-of-deformation changed from almost constant (fbl) to continually slow-increasing (fdl, fal, ffl, fcl). In the second group, specimens f2e, f2f, and f2l are the specimens that experienced almost constant rate-of-deformation after the period of very high rate-of-deformation, and this is not attributed to the change of the impact velocity.

In examining the interface stress-time plots of SIFCON, it has been found that the stress equilibrium condition along the length of specimen is barely satisfied. The delayed rise of the transmitted pulse as well as the higher ratio of length to diameter may account for this.

In Figure 4-11 the first and the second curves, which are stress-strain relations for specimen fe in the first and the fifth impact of same impact speed, resemble each other in the shape and magnitudes. The curve of the fifth test showed higher slope and slightly larger

deformation at the end of loading than that of the first test. The specimen showed no apparent damage after seven impacts in a row, except a coarser cylinder surface representing slightly loosened matrix, which may be caused by lateral expansion of the specimen. Permanent deformation of 1.97% was measured after the seventh impact. Specimen fe was the only specimen in the first group which did not show a strain-softening regime. The drop of the curve was caused by the end of the $300\mu s$ loading pulse and not by specimen failure.

The rest of the group 1 specimens all showed a descending stress regime and experienced damages in a variety of degree. Although, some of the first batch specimen had maximum stress in the stress-strain curve, the trend is elusive in corresponding to the impact velocities and strain rates. The damages involved were matrix loosening, lateral swelling, and shear failure. A damage process may be conjectured as: matrix loosening began around the edge of the cylinder ends, where fiber may be leaner and subjected to larger deformation; then shear failures followed originating from the matrix loosening site(s) and extending along the specimen diagonal direction.

Figures 4-13 show the post-impact pictures of specimen ff1 and fc1. A very clear matrix loosened site and a shear failure originated from that matrix loosened site can be observed on the picture of specimen ff1. Matrix loosened sites and lateral swelling as well as a less obvious shear failure on the face of the cylinder are evident in the picture of specimen fc1.

For group 2, there were no apparent damages for most specimens. Two specimens (f2i, f2e) had very minor matrix loosened site(s) on the

edge. Figure 4-13 shows the remaining steel fibers on the top front edge of the cylinder of specimen f2i. Specimen f21 was the only specimen in this group which had serious matrix loosening damage and shear failures and also had a descending regime in the stress-strain curve.

The scattering of dynamic impact strengths of SIFCON is believed due to the steel fiber distribution and fiber orientation in the specimen. Because of the process used in molding, the fibers tend to have a preferential orientation and are in a layered fashion. Also, due to the mold geometry and rain-in process a uniform fiber distribution is not always guaranteed. As reported by Cheney [4], the static compressive and flexural behavior of SIFCON are highly dependent on the fiber orientation. The difference can be as high as several times. In using SIFCON, steel fiber orientations have to be assured beforehand. And it has been recommended by Cheney that the fibers should be oriented normal to the loading direction.

Although some of the SIFCON specimens were subjected to higher impact speeds than the WES specimens, it is found that the maximum stresses reached in the current experiments on SIFCON ($\approx$170 MPa) are not as high as that of the WES high strength concrete specimens ($\approx$240 MPa). The reason that higher stresses were not attained in the SIFCON is that the SIFCON has a much lower mechanical impedance than the incident pressure bar. This causes much of the incident compressive stress pulse to be reflected as a tensile pulse and not so much transmitted into the specimen as compared with the impacts on the WES concrete. The low mechanical impedance is apparently caused by a very

Figure 4-13. Post-impact picture of specimens ff1 (upper), fc1 (lower) and f21.

Figure 4-13. continued.

low modulus of elasticity in the axial direction. The modulus was, however, not measured accurately in these tests. The highest strain reached by SIFCON was four times more than that of WES specimens. Maybe the strain energy or work of failure should also be employed in representing the capabilities of a material. In considering the safety of constructions, SIFCON may be the better option as compared to un-reinforced concrete for its ductile behavior and the capability in maintaining structural integrity after impact loadings. Nevertheless, the control of fiber orientation is critically important in using SIFCON. It would be advisable to develop a controllable rain-in process which is able to orient the fiber directions and thus furnish a reliable property prediction.

From the previous discussion, ductile behavior of cementitious material can be achieved from the incorporation of short steel fibers. In order to obtain higher fiber volume fraction of a fiber-reinforced material system, study on how to compact fiber seems important. In Milewski's study the problems associated with the nature of short fibers, control of the aspect ratio, and the optimum length of short fibers have been addressed [27]. It will be interesting to review his recommendations and results and make application of his study toward the improvement of steel fiber packing efficiency and achieve the increase of toughness of the steel-fiber-reinforced concrete.

4.1.4 Conclusions

Short-steel-fiber-reinforced concrete specimens made with slurry infiltrated preforms were tested with the SHPB, and complete dynamic

stress-strain curves were obtained. The rough surface of these specimens had effects on the transit time of the transmitted pulse and may have negative influences on the interpretation of test results. It also makes it impossible to use surface strain gages on these specimens. Despite these difficulties damage mechanisms and some useful results were obtained which are believed advantageous in the understanding of this new material system and will pave the way to its future improvements.

The ductility achieved from the incorporation of high fiber volume fraction of SIFCON was shown in these experiments. The uncontrolled distribution and orientation of fibers in specimens were believed to have led to the scattering of the test results. Due to its highly anisotropic characteristics, applications should be based on very careful designing and processing.

4.2 Jacketed Tests of Plain Concrete

4.2.1 Introduction

The stress-strain curves of concrete under complex boundary conditions have been of interest to designers for many years. It is known that concrete may have markedly different behavior under laterally confined or loaded conditions from that of a uniaxial compression test. While plenty of studies have been done statically, with many different loading techniques, on the multi-axial behavior of concrete [1,20,28,29,30], little has been carried out dynamically.

Split Hopkinson pressure bars were employed by Christensen et al. [7] and Lindholm et al. [23] to study the dynamic response of rocks

under radial active confining pressures. Pressure vessels were used in both investigations to obtain pre-impact radial confining pressures.

A passive confining jacket system provides an inexpensive method to experimentally study multi-axial compressive response of concrete specimens. Recent studies by Felice et al.[11] and Gaffney et al.[13] were performed with passive confining jackets and the SHPB to investigate the high strain-rate behavior of soil specimens which were contained in the jackets. Both studies considered that with 60.35 mm inside diameter and 102 mm outside diameter the jacket circumferential deformations are negligible, and the soil specimens are assumed deformed uniaxially. This assumption was further discussed in their studies, and it is believed that the confining jackets do experience radial expansion.

In the present study, thick-wall (31.5 mm) jackets made respectively of aluminum and steel are employed as confining systems. Circumferential deformations of jackets are measured with surface strain gages and recorded with an electronic digital oscilloscope. Problems encountered with jacketed concrete specimens are addressed. The axial stress-strain curves of plain concrete specimens under impact loads and passive confining pressures are determined.

4.2.2 Experiments and Results

In preparing concrete specimens, there are two standard mold sizes that can be chosen from. Their respective dimensions are 76.2 mm and 152.4 mm in diameter and 152.4 mm and 304.8 mm long. For the

present passive confining tests the concrete specimen should have
76.5±0.05 mm diameter to achieve snug-fit with the jackets. Neither
of the standard molds can satisfy this need. In addition, roundness
of the specimen periphery and smoothness of specimen surface are
considered essential in such passive confining tests. To meet the
above requirements, a metallic mold was considered to be the proper
choice.

Twelve aluminum molds with inside diameter of 76.5±0.05 mm and
152.4 mm length were made of solid aluminum cylinders at the
Department of Aerospace Engineering, Mechanics, and Engineering
Science, University of Florida. Prior to casting of concrete, a mold
release agent was sprayed on the inside wall of the aluminum molds.
In the casting of concrete cylinders, the aluminum molds were seated
inside a carton or wooden box, which provides a bottom-stop to contain
the concrete mix during casting and the first 24 hours of curing. A
piece of plastic sheet was placed underneath the molds inside the box
to avoid moisture or water absorption by the box material. Plastic
bags were placed on the top of each individual mold after vibration in
order to protect against excess drying. The mix of the concrete
cylinders is listed in Table 4-2.

After 24 hours in-mold curing, the cast was pushed out of the
molds with a hydraulic jack. Each cylinder was cut into two nominally
50.8-mm-long specimens with a diamond saw after 27 days cure in the
moisture room. Specimens were further ground on both end surfaces to
ensure their smoothness and parallelism.

Table 4-2. Mix of plain concrete specimens.

```
Water/Cement Ratio  ························  0.38
Type II Portland Cement  ····················  38.3 kg
Brooksville stone  ·························  88.3 kg
Kenka sand  ·······························  71.2 kg
Water reducer
    (WRDA - 79)  ·························  5.06 fl oz
Air entrainer  ··························· 0.135 fl oz
Water  ··································  14.5 kg
Air  ····································  5.0 %
21-day average strength of four
    152.4x304.8 mm cylinders  ·············  52.4 MPa
One cubic yard with slump 63.5 mm.
```

The densities of specimens cast from aluminum molds were checked against those of the standard carton molds (76.2x152.4 mm). The respective average densities are 2283 kg/m^3 for eight specimens from aluminum molds and 2275 kg/m^3 for twenty specimens from regular carton molds. All of these specimens were cast with same concrete mix.

Two jackets, made of aluminum and steel with the same dimensions (76.5±0.05 mm I.D., 108.0 mm O.D., 61.0 mm long), were used for the present confining system. With the nominal 50.8-mm-long (2") specimens, approximately 5.1 mm (0.2") of the jacket overlapped the ends of the incident and transmitter bars. This configuration provides supports for the jackets. Two strain gages (Micro-Measurement CEA-06-500UW-350) were mounted circumferentially 180 degrees apart in the middle length of the jacket surface to measure circumferential deformation of jackets in the impact test.

The equation used in the conversion of the measured strains to confining pressures was derived with plane strain elasticity

assumption for the jacket. The relation of the internal pressure p_i and outer surface strain ϵ_t of a thick wall cylinder can be found from [31] and expressed as

$$p_i = E (b^2 - a^2) \epsilon_t]/2a^2,$$

where E is the Young's modulus and a and b are inner and outer diameter of the jacket. Assuming that no gap exists between the specimen and the jacket, the internal pressure in the above equation can be considered as the confining pressure in the jacket-confined tests.

Tests were conducted on two batches of specimens with a total of 20 specimens made by aluminum molds and 10 specimens made by carton molds. Specimens made by carton molds were tested with no confinement. In the first batch, four specimens, two of them made by aluminum molds and the other two by carton molds, were tested quasi-statically at three different loading rates. Quasi-static tests were also carried out on the first batch of the confined test specimens after dynamic impact testing. However, only the permanent deformations were measured for the second batch. All test data are listed in Tables 4-3,4,5 along with part of the test results. Raw strain pulses of two specimens (jab, jsb) recorded from the SHPB are shown in Figures 4-14. Interface velocities and stresses of specimens jab and jsb are given in Figures 4-15 and 4-16. Figure 4-17 gives the average stress, strain rate, and strain versus time curves of the same specimens presented in the previous figures. Stress-strain curves for all specimens are given in Figures 4-18,19,20 and 4-21,22,23.

Confining pressures, which were calculated from the average of two recorded circumferential strains of second batch tests from, respectively, aluminum and steel jackets are shown in Figure 4-24.

Table 4-3. Results of the first batch of confined tests.

SPECIMEN I.D.	IMPACT VELOCITY (m/s)	RESIDUAL STATIC STRENGTH* (MPa)	MAX. STS (MPa)
jaa	7.69	37.95	--
jab#	9.31	28.22	--
jac	9.31	31.26	--
jad	9.98	28.22	--
jae	11.32	26.15	--
jsa	7.39	35.12	--
jsb	9.27	30.50	--
jsc	10.06	30.36	--
jsd	11.45	24.36	--
jse	12.58	24.22	--
jka	7.45	--	101.4
jkb	9.18	--	112.3
jkc	9.91	--	116.2
jkd	11.45	--	120.5

\# Initial confinement was shown not achieved in the non-corrected transmitted pulse.

* Tested at strain rate of $2.5 \times 10^{-4} s^{-1}$.

Table 4-4. Results of quasi-static test of intact specimens.

SPECIMEN I.D.	STRAIN RATE (1/S)	MAX. STRENGTH (MPa)
ia	2.5×10^{-5}	31.05
ib	2.5×10^{-4}	30.02
ic	2.5×10^{-4}	29.88
id	2.5×10^{-3}	34.64

Table 4-5. Results of the second batch of confined tests.

SPECIMEN I.D.	IMPACT VELOCITY (m/s)	PERMANENT DEF. (%)	MAX. STS (MPa)
ja1	7.78	0.18	--
ja2	8.47	0.22	--
ja3	9.44	0.33	--
ja4	10.30	0.42	--
js1	6.69	0.17	--
js2	8.46	0.28	--
js3	9.53	0.41	--
js4	10.21	0.43	--
jk1	7.48	--	87.3
jk2	8.19	--	96.5
jk3	9.39	--	105.0
jk4	9.70	--	109.5
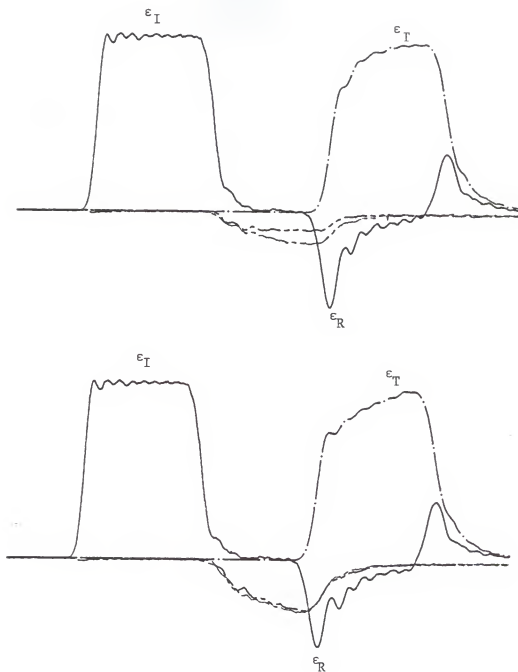
Figure 4-14. Strain pulses in pressure bars of specimen jsb (upper) and jab.
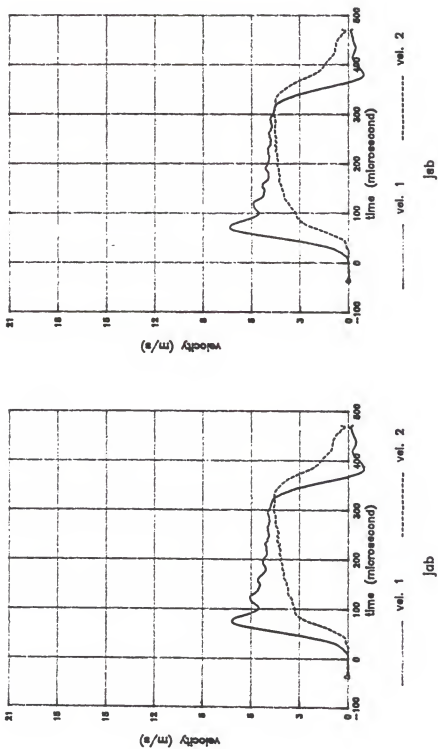
Figure 4-15. Specimen-bar interface velocities of jab and jsb.
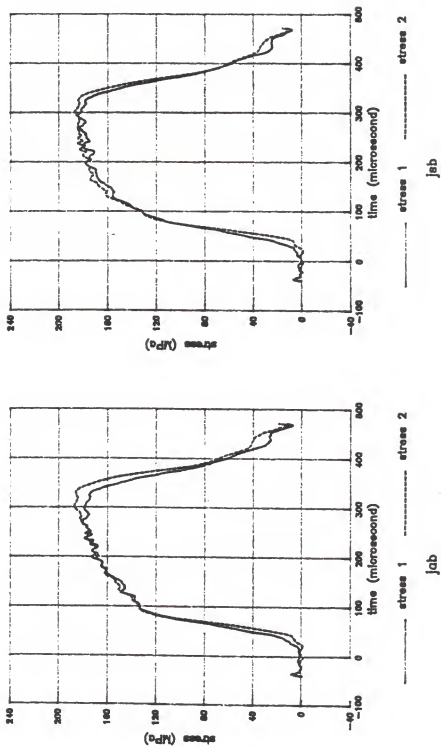
Figure 4-16. Specimen-bar interface stresses of specimens jab and jsb.
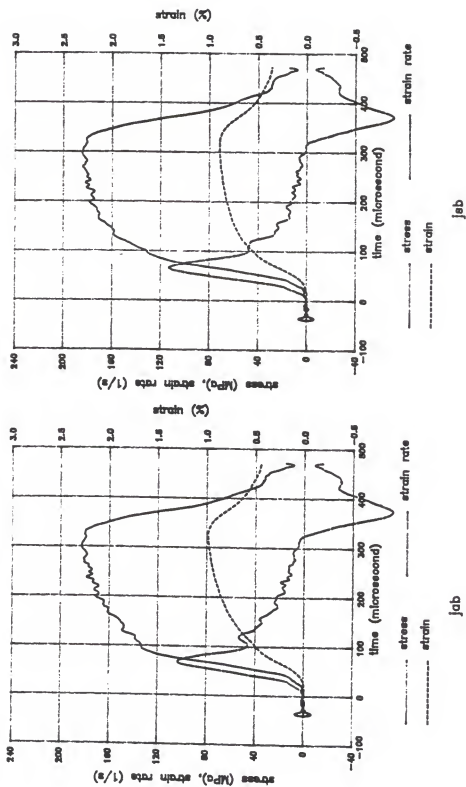
Figure 4-17. Stress (average), strain rate, and strain versus time of jab and jsb.
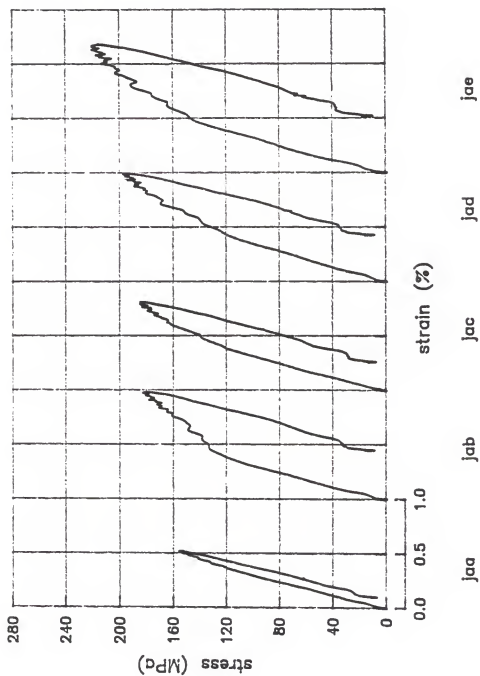
Figure 4-18. Stress-strain curves of the first batch
specimens with aluminum jacket confinement.
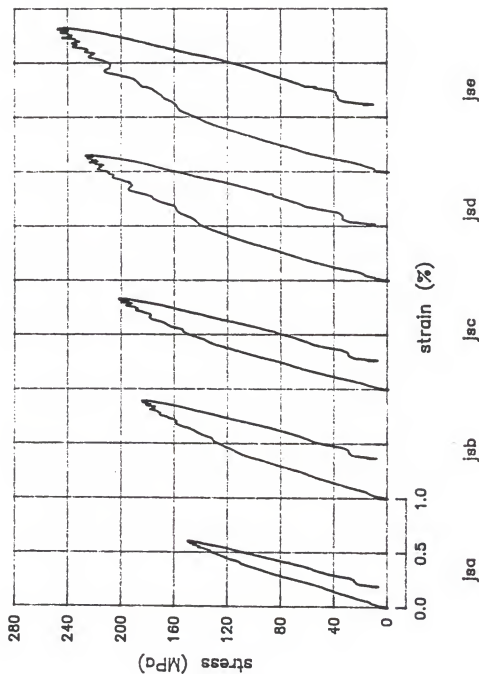
Figure 4-19. Stress-strain curves of the first batch specimens with steel jacket confinement.
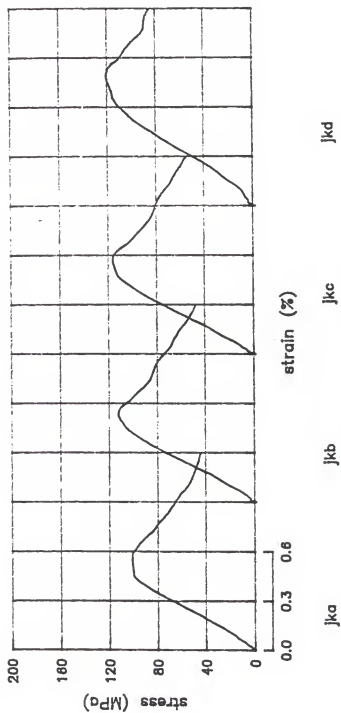
Figure 4-20. Stress-strain curves of the first batch specimens with no confinement.

Figure 4-21. Stress-strain curves of the second batch specimens with aluminum jacket confinement.

Figure 4-22. Stress-strain curves of the second batch specimens with steel jacket confinement.
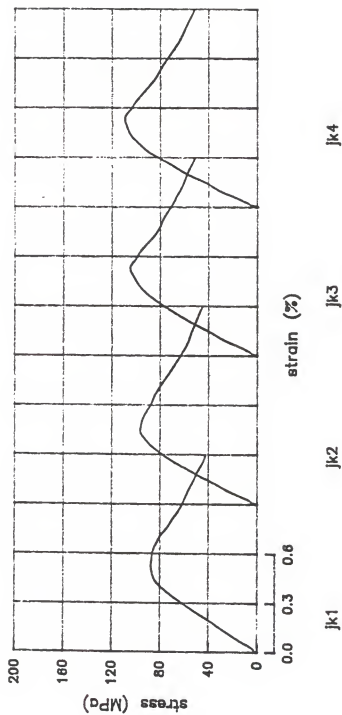
Figure 4-23. Stress-strain curves of the second batch specimens with no confinement.
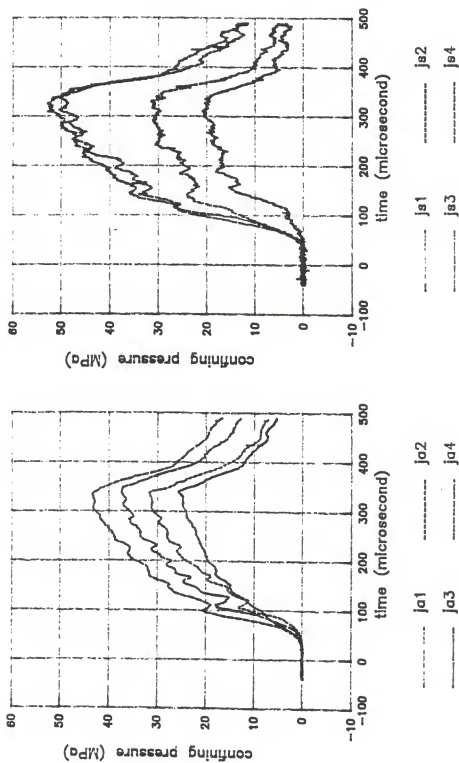
Figure 4-24. Confinement pressures of the second batch tests.

4.2.3 <u>Discussion</u>

For the present confining system, ideally the specimen should be under uniform axial and radial deformation. However, the circumferential strains measured from the confining jackets did not show consistent results. Discrepancies were fou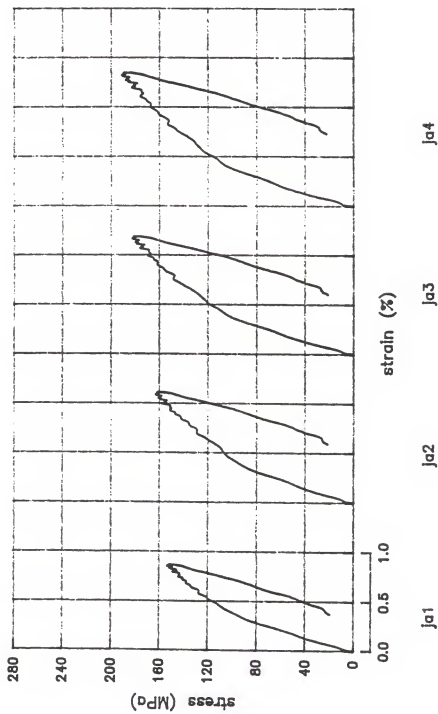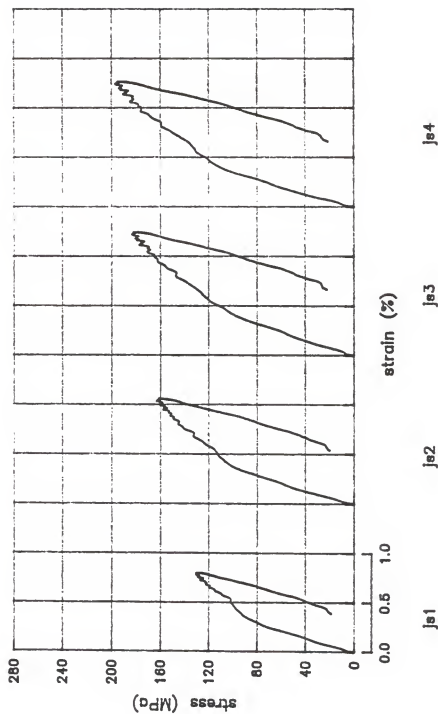nd in several tests. It has been found that the differences between the two circumferential strain gage measurements on the aluminum jacket are much less than that obtained from the steel jacket in the first batch tests. This is considered due to the roughness of the jacket inside surface, which was caused by machining difficulties in fabricating the jacket with inside diameter of 76.5±0.05 mm out of 76.2 mm I.D. steel tube. A second steel jacket, on which efforts had been made to minimize possible roughness, was employed in the second batch tests. The difference between the two measured circumferential strains in all second batch tests was found significantly reduced.

In doing passive confinement tests of concrete specimens with jackets of this type the initial confining pressure induced from the jacket is very difficult to achieve. In addition to smoothness and roundness of the inside surface of the jacket the dimension and surface characteristics of the specimen are crucial as well. Specimens made by molds fabricated from other than metallic materials are unable to fulfill the requirements of this type of passive confinement test. It is difficult to tell quantitatively whether the specimen is adequately smooth and round and capable of fulfilling the required snug-fit condition.

Prior to the test of specimens made by aluminum molds, a batch of

specimens made by regular carton molds (76.2x152.4 mm) were tested with the same jacket used for aluminum-mold-made specimens [24]. With 0.3 mm tolerance the snug-fit condition was apparently not achievable. In those tests it was found that a clear drop in stress followed immediately the initial rise of the transmitted pulse. This drop shows the softening of the specimen and indicates that a gap exists between specimen and jacket. Whether there is a drop right after the rise of the transmitted pulse was used as a criterion in telling if the specimen had experienced initial confining pressure. And it was observed that according to this criterion most tests of specimens made with aluminum molds had achieved the snug-fit requirement.

All confined test specimens maintained their integrity after impact. A criterion or criteria to characterize the effects of impact loadings is needed. For the first batch specimens, quasi-static tests were performed after the impact test. Due to lack of suitable testing equipment, static tests were conducted several months later. During this period the specimens were kept in laboratory with no special insulation or attention.

It seemed that for all static tests failures were initiated at a certain position corresponding to the test jig. That is believed to be caused by the uneven loading conditions which may in turn be due to rough vertical traveling of the test jig. Although the failure pattern was unsatisfactory, static tests of post-impact specimens showed a trend that the residual strength decreases with the increases of impact velocity.

Several specimens showed higher post-impact residual strength than the static strength of intact specimens (Table 4-3,4). These specimens had been subjected to comparatively lower impacts. Whether the impact loads compact the specimen and affect its subsequent static strength may need further experiment and study. Specimens subjected to higher impact speeds showed much lower residual static strength. The reduction of residual strength may be attributed to internal damages that had occurred in the impact test. Specimen jab, which had not had initial confinement in the impact test, showed exceptionally low residual strength. It is believed that for those specimens which do not obtain the snug-fit conditions, much more internal damage may develop in the specimen during the dynamic impact test.

For the second batch tests, which appeared to have had more uniform confinement pressures, the permanent deformations were measured for each specimen. It was found that the permanent deformation increased as higher impact velocities were employed.

It is shown in Figure 4-16 that the first and second interface stresses agreed closely, indicating that the axial stress in the passively confined tests was nearly uniform.

In Figures 4-15 and 4-17, it can be found that the deformation and deformation rate of confined tests decreased after the initial $100\mu s$. The total deformation of specimen jab (Fig. 4-17) in the initial $100\mu s$ period is as much as that of the remaining $240\mu s$ loading duration. And for specimen jsb, the total deformation of the initial $100\mu s$ is larger than that of the remaining loading period. It can be concluded that a concrete specimen in a passively confined experiment

is severely deformed in the beginning loading period. In this period it is believed that the voids that pre-existed in the specimen are crushed and the specimen is compacted. After this voids crushing period the specimen may be further deformed associated with the further elastic deformation of the confining jacket through the rest of loading. The elastically deformed jacket may recover toward its original dimension after the impact, so that the specimen is circumferentially reloaded.

Apparent bend areas can be found on the stress-strain curves of all jacketed tests except jaa and jsa in Figures 4-18,19,20 and 4-21,22,23. Specimen jab, which had not attained initial confinement, had more pronounced bend over area than the other tests in the same group. This bend area may be related to the finish of crushing of pre-existing voids in the specimen. The stresses at bend areas are much higher than the maximum stresses of the corresponding unconfined tests (Fig. 4-20, 4-23).

It is believed that the jacket provides an entirely different deformation pattern for a porous brittle specimen from that of an unconfined test. The pre-existing voids and micro cracks in the concrete specimen play an important role in a confined and an unconfined test. In the unconfined test the pre-existing voids and cracks may serve as the starters of the subsequent damages, while in the confined test these voids or cracks are crushed and compacted.

It was anticipated that due to the difference of the Young's modulus of steel and aluminum ($\approx 3:1$) the confining pressures attained from the two jackets would be highly distinguishable if specimens are

subjected to the same striker-bar impact speed. From Figure 4-24 and Table 4-5, it can be found that confining pressures do not show much difference for approximately the same impact speed tests. And it was found that the circumferential deformations of steel and aluminum jackets were approximately in a ratio of 1:3 for impact speeds of the same range.

The maximum stresses occurred at the inner surface and the maximum strains reached at the outer surface were orders below the yielding stresses and yielding strains of steel and aluminum. No plastic deformation or strain harding effects were taken into account.

4.2.4 Conclusions and Recommendations

A dynamic passive confining experiment of plain concrete specimens using steel and aluminum jackets was successfully performed. The following conclusions could be made from test results 1. Metallic molds proved to be able to produce quality surface and round specimens for jacketed confinement tests. 2. Only with smooth and round inside surface of jacket can the uniform confining pressure be guaranteed. 3. Surface strain gages mounted at two or more different circumferential positions on the jacket can be used to find out the confining pressures and to check the uniformity of the confining pressure as well. 4. The transmitted pulse is evidently useful in serving as a criterion on the snug-fit requirement. 5. Permanent deformation and post-impact residual static strength can be used in characterizing the damage of passive confined test specimens.

There are several aspects interesting to be further explored
1. More specimens can be tested to see how the lower velocity impact
affects the subsequent residual static failure strength. Whether the
low velocity impact compacts the specimens and increases their static
residual strengths should be an interesting question. 2. If the pre-
existing voids and cracks volume fraction can be found somehow, there
may be some kind of relationship between this volume fraction and the
permanent deformation of a passively confined test specimen. It is
believed that for a rigidly confined test the void volume fraction may
provide the limit of a specimen's permanent deformation. 3. Active
confinement in a hydraulic pressure cell may furnish more information
on failure of concrete under controllable amounts of confining
pressure.

CHAPTER 5
SUMMARY AND CONCLUSIONS

In many occasions the actual testing of the functionality of protective structures, primarily made of concrete, to protect against explosive or impact loading is difficult or impossible to carry out. With the advent of high speed super-computers the entire event of the response of protective constructions to weapons attack or impact by wind-driven objects can be simulated, if a suitable model for the material behavior can be formulated. This would be much less costly than a field experiment. The split Hopkinson pressure bar (SHPB) system is a very useful testing apparatus in determining the ultimate dynamic compressive strength of concrete. Test results obtained from the SHPB may be useful for engineers in developing model constitutive equations which are capable to describe the response of concrete under dynamic loads or at high strain-rate loading conditions. These constitutive equations which include high strain-rate response are of interest to structural designers and are indispensible for successful designs of cementituous protective structures.

The present studies began with the dispersion investigation of elastic wave propagation in the split Hopkinson pressure bars in order to correct the data obtained in extensive tests of the uniaxial dynamic compressive response of high strength concrete, short steel fiber reinforced concrete, and laterally passively confined specimens

129

of plain concrete. The wave dispersion was calculated by two methods, one using Fourier series and one using the Fast Fourier Transform (FFT), both based on the Pochhammer-Chree analysis for the individual harmonic components of the propagating pulses. The following conclusions can be drawn from these studies.

1. Wave dispersion in a long cylinder under axial impact causes the lagging of higher frequency components, which can be accounted for by a procedure based on the Pochhammer-Chree analysis for the individual harmonic components.

2. With an IBM-XT-compatible personal computer, the FFT dispersion correction takes about one-tenth the running time of the Fourier series method, and should have less round-off error.

3. More accurate results of concrete tests with the SHPB were obtained with the dispersion correction technique.

4. Surface strain gages were shown very helpful in portraying the failure process in dynamic concrete specimen testing.

5. It is essential to ensure the stress uniformity along the specimen and that no shock wave effects occur in the SHPB test. This can be achieved through the control of the specimen size and the loading rate.

6. The dynamic failure strengths were higher than the static failure strengths for the concrete tested.

7. Slurry infiltrated fiber concrete specimens showed much ductile behavior under impact loads and were able to maintain their integrity for most of the specimens tested.

8. Higher strengths were shown in dynamic tests of metallic-mold-made concrete specimens passively confined with aluminum and steel jackets than in unconfined tests.

A considerable amount of further study of the dynamic response of concrete is needed before a reliable constitutive model can be developed that will accurately predict the dynamic response under confined conditions of multiaxial loading. It is recommended that further study of the response of laterally confined specimens in the SHPB be made with a confining pressure cell, which could provide a more controllable lateral pressure than was provided by the jacketed specimens.

REFERENCES

1. Ahmad, S.H. and Shah, P.S., "Complete Triaxial Stress-Strain Curves for Concrete," Journal of Structural Division, Proceedings, American Society of Civil Engineers, Vol. 108, No. ST4, April 1982, pp. 728-742.

2. Bancroft, D., "The Velocity of Longitudinal Waves in Cylindrical Bars," Physical Review, Vol. 59, 1941, pp. 588-593.

3. Bhargava, J. and Rehnstrom, A., "Dynamic Strength of Polymer Modified and Fiber-Reinforced Concretes," Cement and Concrete Research, Vol. 7, 1977, pp. 199-208.

4. Cheney, S.M., "SIFCON Information and Material Properties," TN 86-04, Air Force Weapons Laboratory, Kirtland Air Force Base, Albuquerque, New Mexico, 1986.

5. Cochran, W.T. et al., "What is the Fast Fourier Transform?", IEEE Transactions on Audio and Electroacoustics, Vol. AU-15, No. 2, 1967, pp. 45-55.

6. Cooley, J.W., Lewis, P.A.W., and Welch, P.D., "Historical Notes on the Fast Fourier Transform," IEEE Transactions on Audio and Electroacoustics, Vol. AU-15, No. 2, June 1967, pp. 76-79.

7. Christensen, R.J., Swanson, S.R., and Brown, W.S., "Split-Hopkinson-Bar Tests on Rock under Confining Pressure," Experimental Mechanics, November 1972, pp. 508-513.

8. Cooley, J.W., Lewis, P.A.W., and Welch, P.D., "Application of the Fast Fourier Transform to Computation of Fourier Integrals, Fourier Series, and Convolution Integrals," IEEE Transactions on Audio and Electroacoustics, Vol. AU-15, No. 2, June 1967, pp. 79-84.

9. Davies, E.D.H., "A Critical Study of the Hopkinson Pressure Bar," Philosophical Transactions A, Vol. 240, 1948, pp. 375-457.

10. Felice, C.W., "The Response of Soil to Impulse Loads Using the Split-Hopkinson Pressure Bar Technique," AFWL-TR-85-92, Final Report, Air Force Weapons Laboratory, Kirtland Air Force Base, New Mexico, May 1986.

11. Felice, C.W., Brown, J.A., Gaffney, E.S., and Olsen, J.M., "An Investigation into the High Strain-Rate Behavior of Compacted Sand Using the Split-Hopkinson Pressure Bar Technique," Second Symposium on the Interaction of Non-Nuclear Munitions with Structures, Panama City Beach, Florida, April 15-19, 1985.

12. Follansbee, P.S. and Frantz, C., "Wave Propagation in the Split Hopkinson Pressure Bar," Journal of Engineering Materials and Technology, Vol. 105, January 1983, pp. 61-66.

13. Gaffney, E.S., Brown, J.A., and Felice, C.W., "Soils as Samples for the Split Hopkinson Bar," Second Symposium on the Interaction of Non-Nuclear Munitions with Structures, Panama City Beach, Florida, April 15-19, 1985.

14. Glenn, L.A. and Janach, W., "Failure of Granite Cylinders under Impact Loading," International Journal of Fracture, Vol. 13, No. 3, June 1977, pp. 301-317.

15. Goldsmith, W., Polivka, M., and Yang, T., "Dynamic Behavior of Concrete," Experimental Mechanics, February 1966, pp. 65-79.

16. Graham, D.E., "Determining the Static and Dynamic Properties of Hardened Normal Weight and Heavy Weight Concrete," Cement, Concrete, and Aggregates, CCAGSP, Vol. 8, No. 2, Winter 1986, pp. 57-67.

17. Hannant, D.J., Fiber Cements and Fiber Concretes, John Wiley & Sons, Chichester, England, 1978.

18. Kolsky, H., "An Investigation of the Mechanical Properties of Materials at Very High Rates of Loading," Proceedings of the Physical Society, B, Vol. 62, 1949, pp. 676-701.

19. Kolsky, H., Stress Waves in Solids, Dover Publications, New York, 1963.

20. Kotsovos, M.D. and Newman, J.B., "Behavior of Concrete Under Multiaxial Stress," ACI Journal, September 1977, pp. 443-446.

21. Lankard, D.R., "Slurry Infiltrated Fiber Concrete (SIFCON)," Concrete International, December 1984, pp. 44-47.

22. Lankard, D.R. and Lease, D.H., "Highly Reinforced Precast Monolithic Refractories," American Ceramic Society Bulletin, Vol. 61, No. 7, July 1982, pp. 728-732.

23. Lindholm, U.S., Yeakley, L.M., and Nagy, A., "The Dynamic Strength and Fracture Properties of Dresser Basalt," Int. J. Rock Mech. Min. Sci. & Geomech. Abstr., Vol. 11, 1974, pp. 181-191.

24. Malvern, L.E., and Ross, C.A., "Dynamic Response of Concrete and Concrete Structures," Final Report, AFOSR F49620-83-k007, University of Florida, Gainesville, Florida, May 1986.

25. Malvern, L.E., Tang, T., Jenkins, D.A., and Gong, J.C., "Dynamic compressive strength of cementitious materials," in Cement-Based Composites: Strain Rate Effects on Fracture, Materials Research Society Symposia Proceedings, Vol. 64, S. Mindess and S.P. Shah, Ed., MRS, Pittsburgh, PA, 1986, pp. 119-138.

26. McHenry, D. and Shideler, J.J., "Review of Data on Effect of Speed in Mechanical Testing of Concrete," ASTM STP 185, pp. 72-82, 1956.

27. Milewski, J.V., "Efficient Use of Whiskers in the Reinforcement of Ceramics," Advanced Ceramic Materials, Vol. 1, 1986, pp. 36-41.

28. Mills, L.L. and Zimmerman, R.M., "Compressive Strength of Plain Concrete Under Multiaxial Loading Conditions," ACI Journal, October 1970, pp. 802-807.

29. Newman, J.B., Concrete under Complex Stress, Chapter 5, Developments in Concrete Technology, Edited by F.D. Lydon, Applied Science Publishers LTD, London, 1979.

30. Tasuji, M.E., Slate, F.O.., and Nilson, A.H., "Stress-Strain Response and Fracture of Concrete in Biaxial Loading," ACI Journal, July 1978, pp. 306-312.

31. Timoshenko, S., Strength of Materials. Part II, 3rd Edition, D. Van Nostrand Company, Inc., New York, New York, March, 1956.

32. van Elst, H.C., "The evaluation of the decrease in resistance against crack propagation in steel by embrittlement using a stress wave attenuation test," in Dynamic Crack Propagation, edited by Sih, G.C., 1972.

33. Watstein, D., "Effect of Straining Rate on the Compressive Strength and Elastic Properties of Concrete," Journal of the American Concrete Institute, Vol. 24, April 1953, pp. 729-744.

34. Yew, E.H., and Chen, C.S., "Experimental Study of Dispersive Waves in Beam and Rod Using FFT," Journal of Applied Mechanics, Vol. 45, December 1978, pp. 940-942.

35. Young, C. and Powell, N., "Lateral Inertia Effects on Rock Failure in Split-Hopkinson-Bar Experiments," 20th U.S. Symposium on Rock Mechanics, 1979.

Jyh-Cherng Gong was born in Chaiyi, Taiwan, Republic of China, on November 27, 1955. He was graduated with a Bachelor of Science degree in aeronautical engineering at Tamkang University, Tamsui, Taiwan, in June of 1978. He came to the United States of America and enrolled in the Department of Mechanical and Aerospace Engineering at the State University of New York at Buffalo as a graduate student in August, 1981. In August, 1983 he finished his Master of Science degree at SUNY Buffalo, New York. Since then he has worked toward his doctoral degree at the University of Florida in the Department of Aerospace Engineering, Mechanics, and Engineering Science with a major in Engineering Mechanics.

I certify that I have read this study and that in my opinion it conforms to acceptable standards of scholarly presentation and is fully adequate, in scope and quality, as a dissertation for the degree of Doctor of Philosophy.

Lawrence E. Malvern, Chairman
Professor, Aerospace Engineering,
Mechanics, and Engineering Science

I certify that I have read this study and that in my opinion it conforms to acceptable standards of scholarly presentation and is fully adequate, in scope and quality, as a dissertation for the degree of Doctor of Philosophy.

Chang-Tsan Sun
Professor, Aerospace Engineering,
Mechanics, and Engineering Science

I certify that I have read this study and that in my opinion it conforms to acceptable standards of scholarly presentation and is fully adequate, in scope and quality, as a dissertation for the degree of Doctor of Philosophy.

Charles E. Taylor
Professor, Aerospace Engineering,
Mechanics, and Engineering Science

I certify that I have read this study and that in my opinion it conforms to acceptable standards of scholarly presentation and is fully adequate, in scope and quality, as a dissertation for the degree of Doctor of Philosophy.

Chen-Chi Hsu
Professor, Aerospace Engineering,
Mechanics, and Engineering Science

I certify that I have read this study and that in my opinion it conforms to acceptable standards of scholarly presentation and is fully adequate, in scope and quality, as a dissertation for the degree of Doctor of Philosophy.

Arun K. Varma
Professor, Mathematics

This dissertation was submitted to the Graduate Faculty of the College of Engineering and to the Graduate School and was accepted as partial fulfillment of the requirements for the degree of Doctor of Philosophy.

August, 1988

Dean, College of Engineering

Dean, Graduate School